

# Transport Pathways of Peroxyacetyl Nitrate in the Upper Troposphere and Lower Stratosphere from different monsoon systems during the Summer Monsoon Season

Suvarna Fadnavis<sup>1</sup>, Kirill Semeniuk<sup>2</sup>, Martin G. Schultz<sup>3</sup> and Michael Kiefer<sup>4</sup>, Anoop Mahajan<sup>1</sup>, Luca Pozzoli<sup>5</sup>, S. Sonbawane<sup>1</sup>

<sup>1</sup>Indian Institute of Tropical Meteorology, Pune India

<sup>2</sup>Department of Earth and Space Sciences and Engineering, York University, Toronto, Canada

<sup>3</sup>Institute for Energy and Climate Research-Troposphere (IEK-8), Forschungszentrum Jülich, Jülich, Germany

<sup>4</sup>Karlsruhe Institute of Technology, Institute for Meteorology and Climate Research, Karlsruhe, Germany

<sup>5</sup>Eurasia Institute of Earth Sciences, Istanbul Technical University, Turkey

## Abstract:

The Asian summer monsoon involves complex transport patterns with large scale redistribution of trace gases in the upper troposphere and lower stratosphere (UTLS). We employ the global chemistry-climate model ECHAM5-HAMMOZ in order to evaluate the transport pathways and the contributions of nitrogen oxide species PAN, NO<sub>x</sub>, and HNO<sub>3</sub> from various monsoon regions, to the UTLS over Southern Asia and vice versa. Simulated long term seasonal mean mixing ratios are compared with trace gas retrievals from the Michelson Interferometer for Passive Atmospheric Sounding aboard ENVISAT( MIPAS-E) and aircraft campaigns during the monsoon season (June-September) in order to evaluate the model's ability to reproduce these transport patterns.

The model simulations show that there are three regions which contribute substantial pollution to the South Asian UTLS: the Asian summer monsoon (ASM), the North American Monsoon (NAM) and the West African monsoon (WAM). However, penetration due to ASM convection reaches deeper into the UTLS as compared to NAM and WAM outflow. The

circulation in all three monsoon regions distributes PAN into the tropical latitude belt in the upper troposphere (UT). Remote transport also occurs in the extratropical UT where westerly winds drive North American and European pollutants eastward where they can become part of the ASM convection and lifted into the lower stratosphere. In the lower stratosphere the injected pollutants are transported westward by easterly winds. Sensitivity experiments with ECHAM5-HAMMOZ for simultaneous NO<sub>x</sub> and NMVOCs emission change (-10 %) over ASM, NAM, WAM confirm similar transport. Our analysis shows that 10% change in Asian emissions, transport ~5-30 ppt of PAN in the UTLS over Asia, ~1-10 ppt of PAN in the UTLS of Northern subtropics and mid latitudes, ~7-10 ppt of HNO<sub>3</sub> and ~1-2 ppb of ozone in UT over Asia. Comparison of emission change over Asia, North America and Africa shows highest transport of HNO<sub>3</sub> and ozone occurs in the UT over Asia and least over Africa.

The intense convective activity in the monsoon regions is associated with lightning and thereby the formation of additional NO<sub>x</sub>. This also affects the distribution of PAN in the UTLS. Simulations with and without lightning show an increase in the concentrations of PAN (~40 %), HNO<sub>3</sub> (75%), NO<sub>x</sub> (70 %) and ozone (30 %) over the regions of convective transport. Lightning induced production of these species is higher over equatorial Africa and America as compared to the ASM region. This indicates that the contribution of anthropogenic emission to PAN in the UTLS over the ASM, is higher than that of lightning.

## 1. Introduction

Deep monsoon convection plays a key role in venting chemical constituents from the boundary layer and their export from source regions (Dickerson et al., 1987). The largest regional monsoon systems are the North American monsoon (NAM), Asian Summer Monsoon (ASM), Western North Pacific monsoon (WNPM), South American monsoon (SAM), West African Monsoon (WAM), and the Australian Monsoon (AUSM) (Chang et al., 2011). Recent observation and modeling studies indicate that the Asian summer monsoon (Park et al., 2004; Li et al., 2005; Randel and Park, 2006; Fu et al., 2006; Park et al., 2007; Xiong et al., 2009; Randel et al., 2010; Fadnavis et al., 2013), the North American Monsoon (Schmitz and Mullen 1996; Collier and Zhang, 2006; Barth et al., 2012) and the West African monsoon (Bouarar et al., 2011) play important roles in the transport of chemical constituents out of the boundary layer into the northern hemisphere in the Upper Troposphere (UT). A Number of studies have documented that large amounts of pollution from Asia are transported across the tropopause (Park, 2006; Fu et al., 2006; Park et al., 2007). However transport from other monsoon systems (WAM, NAM) and their contribution to Asia have so far got less attention. Until now there has been no attempt to assess the relative contributions from these source regions and to analyze the transport patterns including possible recirculation within one consistent model framework. Prior model simulations suggest that pollutants transported from the Asian monsoon region can contribute substantially to the budgets of stratospheric ozone,  $\text{NO}_x$  and water vapour (Randel et al., 2010). Ozone formation in the anticyclone is also enhanced by transport of pollution plumes from the North American monsoon which are rich in volatile organic compounds (VOC) (Li et al., 2005; Zhang et al., 2008; Choi et al., 2009; Barth et al., 2012). The deep monsoon convection over West Africa transports Central African emissions to the upper troposphere and lower

stratosphere (UTLS) leading to large ozone changes in the lower stratosphere (Bouarar et al., 2011). A number of studies have reported transport of chemical constituents into the UTLS due to the Asian monsoon convection, while less attention has been paid to deep convective transport from North/South America and West Africa to the lower stratosphere and to their relative contributions to the UTLS composition over the ASM region.

This study investigates the transport patterns and relative contributions to the Asian monsoon anticyclone of three oxidized nitrogen species, namely peroxyacetyl nitrate (PAN),  $\text{NO}_x$  (the sum of  $\text{NO}$  and  $\text{NO}_2$ ), and nitric acid ( $\text{HNO}_3$ ). PAN is a secondary pollutant that marks the transport and conversion of surface  $\text{NO}_x$  after it is emitted. The focus of this study is placed on PAN as this species has a long lifetime (90-180 days) in the UT and can be favorably observed by satellite instruments. At the same time its short chemical lifetime in the lower troposphere (not longer than 30 days) results in a much tighter association between the emissions regions of its precursors and transport compared to species such as carbon monoxide (CO). The much longer chemical lifetime of CO in the lower troposphere allows it to reach the UTLS via circuitous pathways that are not accessible to PAN. In contrast, PAN is a tracer that allows for a clearer identification of  $\text{NO}_x$  pollution transport pathways between the surface and the UTLS. We perform  $\text{NO}_x$  and MNVOCs emission sensitivity simulations (where emissions of  $\text{NO}_x$  and MNVOCs were simultaneously reduced by 10%) in order to investigate the relative contributions from Asia, Africa and America to the PAN,  $\text{HNO}_3$  and  $\text{O}_3$  concentrations in the UTLS.

PAN is formed through oxidation of non methane volatile organic compounds (NMVOCs) in the presence of  $\text{NO}_x$  (Fischer et al., 2014). It is primarily formed after oxidation of acetaldehyde ( $\text{CH}_3\text{CHO}$ ) or after photolysis of acetone ( $\text{CH}_3\text{COCH}_3$ ) and methyl glyoxal ( $\text{CH}_3\text{COCHO}$ ), all of

which are oxidation products of various NMVOCs. The actual formation of PAN proceeds in the reaction of the peroxy acetyl radical ( $\text{CH}_3\text{CO}_3$ ) with  $\text{NO}_2$ . This reaction is reversible and the thermal decomposition of PAN back to  $\text{CH}_3\text{CO}_3$  and  $\text{NO}_2$  is the main sink of PAN, although in the UTLS PAN photolysis becomes the dominant loss process. Two minor loss processes of PAN are reaction with OH and dry deposition (Talukdar et al., 1995; Fischer et al., 2014). As stated by Fischer et al. (2014) globally, biogenic VOC like isoprene and terpenes contribute most to PAN formation, but in the context of our study it is important to note that the oxidation of many alkanes and alkenes which are emitted from anthropogenic sources lead to PAN formation as well. The major anthropogenic sources of NMVOCs are the emissions from fossil fuel and biofuel combustion and from industrial solvents (Tang et al., 2009). Biomass burning, biogenic and soil emissions also contribute to NMVOC and  $\text{NO}_x$  production. Anthropogenic sources are dominant in the extra tropical Northern Hemisphere outside the spring season. In spring, when surface PAN peaks, biogenic and anthropogenic NMVOCs species are responsible for ~50% of the PAN burden.

In the UT, lightning can add substantial amounts of  $\text{NO}_x$  and thus lead to additional PAN production if NMVOC precursors are present, e.g. from convective uplifting from the boundary layer (Tie et al., 2001). The estimated global  $\text{NO}_x$  production by lightning is ~3 - 5 Tg N/year (Schumann and Huntrieser, 2007; Martin et al., 2007; Murray et al., 2012). Strong lightning activity during ASM, NAM and WAM (Shepon, et al., 2007; Evett et al., 2008; Ranalkar and Chaudhari, 2009; Barret et al., 2010; Penki and Kamra, 2013) hence contributes to PAN production in the UTLS. The estimated increase in PAN is ~20 - 30 % due to  $\text{NO}_x$  enhancement by lightning (Tie et al., 2001).

The thermal decomposition rate of PAN is highly temperature dependent. In the UTLS temperatures are sufficiently low to prevent thermal decomposition of PAN and therefore the chemical lifetime of PAN in this region is ~90 - 180 days (Arnold and Hauck, 1984). The PAN lifetime in our ECHAM5-HAMMOZ simulations varies between 80 days and 170 days in the tropical UTLS. Several studies (Tereszchuk et al., 2013, Glatthor et al., 2007, Sign et al 1987) have reported that the lifetime of PAN varies between 2 - 4 months. PAN thus travels over long distances and affects the NO<sub>y</sub> partitioning in areas that are far away from the precursor emission regions. Upon descent into warmer regions of the troposphere, PAN releases NO<sub>x</sub> which in turn increases ozone and OH production in remote regions (Singh et al., 1986; Singh et al., 1998; Hudman et al., 2004). PAN mixing ratios vary from less than 1 pptv in the remote marine atmosphere (as observed during the NASA GTE PEM-Tropics B campaign in the South Pacific lower marine boundary layer, data available at <http://acd.ucar.edu/~emmons/DATACOMP/>) to several ppbv in the polluted urban environment and biomass burning plumes (Ridley et al., 1992; Singh et al., 1998). In the UTLS mixing ratios are typically in the range 10-300 pptv (Emmons et al., 2000; Keim et al., 2008).

To our knowledge our study is the first study that analyzes the influence of monsoon outflow from different world regions on the distribution of peroxyacetyl nitrate (PAN) in the UTLS over the Asian monsoon region, and its recirculation in the UTLS. We run decadal simulations with the chemistry climate model ECHAM5-HAMMOZ. In emission sensitivity experiments, NO<sub>x</sub> and NMVOCs emissions were simultaneously reduced by 10% over ASM, WAM and NAM to understand regional contribution. We apply statistical comparisons with satellite and aircraft data, thereby contributing to the objectives of the Chemistry Climate Model Initiative (CCMI, see <http://www.igacproject.org/CCMI>). The model climatology is evaluated with data from

aircraft campaigns and the Michelson Interferometer for Passive Atmospheric Sounding (MIPAS) instrument onboard the ENVironmental SATellite (ENVISAT) (Refereed as MIPAS-E hereafter). The transport of  $\text{HNO}_3$  and  $\text{NO}_x$  due to monsoon convection from different monsoon regions and the impacts of lightning on the UTLS distributions of the nitrogen oxides are also analyzed and compared to the results obtained for PAN. The paper is organized as follows: Section 2 contains a short description of the data and model including the simulation setup. Comparisons of model simulations with observations are given in section 3. In section 4, we discuss the various convective transport pathways of PAN into the UTLS, its redistribution in the stratosphere and its re-circulation across the various monsoon regions as well as results of the emission sensitivity simulations depicting contribution from major monsoon systems. The analysis of percentage changes in lightning produced ozone,  $\text{HNO}_3$ , PAN and  $\text{NO}_x$  on total concentrations over the convective zones is presented in section 5. Conclusions are given in section 6.

## 2. Methods

### 2.1 Satellite measurements

MIPAS-E instrument onboard the ENVISAT was launched in March 2002 into a polar orbit of 800 km altitude, with an orbital period of about 100 minutes and an orbit repeat cycle of 35 days. MIPAS-E (Fischer and Oelhaf, 1996; Fischer et al., 2008) was a Fourier Transform Spectrometer that provided continual limb emission measurements in the mid infrared over the range 685 – 2410  $\text{cm}^{-1}$  (14.6 – 4.15  $\mu\text{m}$ ). From January 2005 through the end of the mission in April 2012 MIPAS was operated with a spectral resolution of 0.0875  $\text{cm}^{-1}$ , and a stepping of the tangent altitude of 1.5 – 2 km in the UTLS region. As mid infrared sounder MIPAS-E could not provide spectral information from below cloud top.

MIPAS-E monitored several atmospheric trace constituents affecting atmospheric chemistry including PAN,  $\text{NO}_x$ , and  $\text{O}_3$ . The details of the general retrieval method and setup, error estimates and use of averaging kernel and visibility flag are documented by Von Clarmann et al. (2009). In this study we analyze the MIPAS-E observed PAN data during the period 2005 – 2012, i.e. the data version V5R\_PAN\_220/V5R\_PAN\_221 (different naming 220/221 merely due to technical reasons). The data are available from [http://share.lsd.f.kit.edu/imk/asf/sat/mipas-export/Data\\_by\\_Target/](http://share.lsd.f.kit.edu/imk/asf/sat/mipas-export/Data_by_Target/). Details of the MIPAS PAN retrievals, error budget, and vertical resolution are given by Glatthor et al. (2007) and by Wiese et al. (2012). Table 3 in Wiese et al. (2012) indicates that for the total error of single profiles of the V5R\_PAN\_220/221 product the spectral noise and the uncertainty of the instrument pointing are the main contributors. However, since noise is a major contributor a reduction of the total error can be expected for vertical profiles of binned data. For typical bins used in this work the total errors are less than 10 % below 12 km, 30 % at 15 km, 50 % at 19 km and 80 % at 23 km.



The sensitivity of the PAN retrievals can be judged by the averaging kernels. For the V5R\_PAN\_220/221 product an example of the respective averaging kernel rows is shown in figure S1 for an altitude range of 5 to 25 km at 28 degree N and 85 degree E for cloud free atmospheric conditions. The diamonds indicate the respective nominal altitudes of the retrieval grid. The figure shows that the retrieval results below 8 - 9 km are dominated by information from above the nominal altitude. A similar, albeit less obvious, situation develops for altitudes above 22 - 23 km. There and above the information has an increasing weight from lower than nominal altitudes. This is the reason why the MIPAS PAN data is not considered below 8 km and above 23 km. Another effect clearly visible in the example is that the altitude region which influences the retrieved PAN value at a given altitude is increasing with altitude, i.e. the vertical resolution decreases with altitude. To account for the comparatively low, and altitude dependent, vertical resolution, the model data to be directly compared to MIPAS measurements was convolved with the MIPAS PAN averaging kernel.

The data are contoured and gridded at 4 degree latitude and 8 degree longitude resolution. In the process the data quality specifications as documented at <http://share.lsd.fkit.edu/imk/asf/sat/mipas-export/Documentation/> were employed, namely: only data with visibility flag equal 1 and diagonal value of averaging kernel greater than 0.03 were used.

## **2.2 ECHAM5-HAMMOZ model simulation and experimental setup**

The ECHAM5-HAMMOZ aerosol-chemistry-climate model used in the present study comprises of the general circulation model ECHAM5 (Roeckner et al., 2003), the tropospheric chemistry module, MOZ (Horowitz et al., 2003), and the aerosol module, Hamburg Aerosol Model (HAM) (Stier et al., 2005). It includes ozone, NO<sub>x</sub>, VOC and aerosol chemistry. The gas

phase chemistry scheme is based on the MOZART-2 model (Horowitz et al., 2003), which includes comprehensive  $O_x$ - $NO_x$ -hydrocarbons chemistry with 63 tracers and 168 reactions. The  $O(^1D)$  quenching reaction rates were updated according to Sander et al. (2003), and isoprene nitrates chemistry according to Fiore et al. (2005). In the model simulations we included emissions of acetone from anthropogenic sources and wild fires (primary sources), while acetaldehyde and methylglyoxal are produced by oxidation of other NMVOCs (secondary sources). In particular, oxidation of primary NMVOCs like ethane ( $C_2H_6$ ), propane ( $C_3H_8$ ) and propene ( $C_3H_6$ ) forms acetaldehyde, while  $CH_3COCHO$  is mainly formed from the oxidation products of isoprene and terpenes. Higher acyl peroxy nitrates (MPAN) have been included in the MOZART-2 chemical scheme, which are also formed through oxidation of NMVOCs, but their production is small compared to PAN. Thermal decomposition, and reaction with OH as well as the absorption cross sections for PAN photolysis are all specified according to Sander et al. (2003).

In ECHAM5-HAMMOZ dry deposition follows the scheme of Ganzeveld and Lelieveld (1995). Soluble trace gases such as  $HNO_3$  and  $SO_2$  are also subject to wet deposition. In-cloud and below cloud scavenging follows the scheme described by Stier et al. (2005). PAN is not water soluble, therefore dry and wet deposition are insignificant removal processes.

The model is run at a spectral resolution of T42 corresponding to about  $2.8 \times 2.8$  degrees in the horizontal dimension and 31 vertical hybrid  $\sigma$ -p levels from the surface up to 10 hPa. We note that the nominal grid resolution of 2.8 degrees is somewhat misleading, because the spectral truncation of T42 only allows to resolve details on the order of  $180/42 = 4.28$  degrees. This is the main reason why we compare our model results with the MIPAS PAN retrievals on a  $4 \times 8$

degree grid. The details of model parameterizations, emissions and validation are described by Pozzoli et al., (2008a,b, 2011) and Fadnavis et al. (2013).

The **model** simulations were performed with varying monthly mean sea surface temperature (SST) and sea ice cover (SIC) data over the period 2000 – 2010 (AMIP) referred as control simulation. The simulations did not aim to exactly reproduce specific meteorological years, and we ran 11-year periods in order to obtain a reasonable statistics. We used the RETRO project data set of the year 2000 available at <http://eccad.sedoo.fr/> for the surface CO, NO<sub>x</sub>, and hydrocarbon emissions from anthropogenic sources and biomass burning (Schultz et al., 2004; 2005; 2007; 2008). Anthropogenic total RETRO emissions of the year 2000 are 476 Tg/year for CO and 90 Tg/year for NO<sub>x</sub>, 5 Tg/year of ethane, 3.5 Tg/year of propane and 2.7 Tg/year of propene, which are the main anthropogenic VOC precursors of PAN. Biomass burning RETRO emissions of year 2000 are 357 Tg/year for CO, and 16 Tg/year for NO<sub>x</sub>. 2.5 Tg/year for ethane, 1.3 Tg/year for propane, 2.7 Tg/year for propene, and 2.7 Tg/year for acetone. CO biomass burning emissions in Southeast Asia account for 7 Gg/month in spring, while up to 15 Gg/month were reported from Carmichael et al. (2003). The anthropogenic and biomass burning emissions of SO<sub>2</sub> (total of 142 Tg/year), BC (7.7 Tg/year) and OC (66.1 Tg/year) are based on the AEROCOM emission inventory (Dentener et al., 2006), also representative of the year 2000. The biogenic NMVOC emissions are calculated on-line with the MEGAN module of Guenther et al. (2006). The simulated global annual mean emission of biogenic NMVOCs between 1995 and 2004 is 830 Tg(C)/year, isoprene contributes by 57 %, followed by terpenes (21 %), methanol (12 %), and other NMVOCs such as acetaldehyde (2.5 %) and acetone (2.3 %). Other natural emissions calculated on-line by the model are the Dimethyl Sulfide (DMS) fluxes (Kettle and

Andreae, 2000; Nightingale et al., 2000; Pham et al., 1995), sea salt aerosols (Schulz et al., 2004) from the oceans, and mineral dust aerosols (Tegen et al., 2002; Cheng et al., 2008).

Our base year for aerosol and trace gas emissions is 2000, and emissions were repeated annually throughout the simulation period. One point to note is that there were substantial emission changes in Asia and Africa (increasing trends) and Europe and North America (decreasing trends) during the study period, which is not captured in our simulations. A consequence of these emission changes for our study would be that we may underestimate the impact from local pollution sources on PAN concentrations in the UTLS over the ASM region in recent years and that we overestimate the contribution from long-range transport of northern hemispheric pollution. We provide an estimate of this error in the discussion of the results. Lightning  $\text{NO}_x$  emissions are parameterized following Grewe et al. [2001]. They are proportional to the calculated flash frequency with a production rate of 9 kg(N) per flash, and distributed vertically using a C-shaped profile. The calculated flash frequency is resolution-dependent and scaled globally to yield annual global emissions of 3.4 Tg(N) per year. To study the impact of lightning on the distributions of PAN we compare two sets of experiments; each conducted for 11 years 2000-2010: (1) the control experiment (CTRL) and (2) the lightning off experiment (light-off).

Model simulated PAN,  $\text{NO}_x$ ,  $\text{HNO}_3$  and  $\text{O}_3$  mixing ratios are evaluated with climatological datasets of airborne campaigns during the monsoon season (June-September). The data were retrieved from <http://acd.ucar.edu/~emmons/DATACOMP/CAMPAIGNS/> (see also the paper by Emmons, 2001). The  $\text{NO}_x$  and ozone volume mixing ratios observed during Cloud Aerosol Interaction and Precipitation Enhancement Experiment (CAIPEEX) (details available in

Kulkarni et al., 2012), September 2010, are evaluated over the Indian region. The details of instruments and measurement techniques are available at <http://www.tropmet.res.in/~caipeer/about-data.php>. The list of data sets and aircraft campaign used for comparison are presented in Table 1. For the comparison, aircraft observations are averaged over 0 - 2 km, 2 - 6 km and 6 - 8 km and horizontally over the coherent flight regions.

In order to understand the impact of  $\text{NO}_x$  and NMVOCs emissions on the distribution of PAN, we conducted a reference and 3 emission sensitivity simulations for the year 2003 driven by European Centre for Medium-Range Weather Forecasts operational analyses (Integrated Forecast System (IFS) cycle-32r2) meteorological fields (available every 6 h) (Uppala et al., 2005). Model simulations were performed for the year 2003 since there was no significant oceanic/meteorological perturbation event like, e.g., El Niño Southern Oscillation or the Indian Ocean Dipole ([http://www.marine.csiro.au/~mcintosh/Research\\_ENSO\\_IOD\\_years.htm](http://www.marine.csiro.au/~mcintosh/Research_ENSO_IOD_years.htm)). In experiments 1 to 3, emissions of both  $\text{NO}_x$  and MNVOCs were simultaneously reduced by 10% over (1) Asia ( $10^\circ\text{S}$ - $50^\circ\text{N}$ ,  $60^\circ\text{E}$ - $130^\circ\text{E}$ ), (2) Africa ( $30^\circ\text{S}$ - $30^\circ\text{N}$ ,  $15^\circ\text{W}$ - $45^\circ\text{E}$ ), and (3) North America ( $15^\circ\text{N}$ - $45^\circ\text{N}$ ,  $120^\circ\text{W}$ - $75^\circ\text{W}$ ) separately, refereed as Asia-10%, Africa-10%, North-America-10%.

### 2.3 Model production of PAN

PAN is a secondary pollutant that has a short lifetime in the lower troposphere. This reduces the number of source points that contribute to PAN concentrations at any location in the UTLS resulting in a clearer identification of source-receptor pathways. Figure 1 shows the distribution of PAN production at 14 km and 16 km. A striking feature is the confinement of PAN production to regions of deep convection. A maximum daily production rate of PAN in the UTLS, in these

convective zones, is >24 ppt/day near 14 km and >12 ppt/day near 16 km. Production of PAN from background concentrations of ethane ( $C_2H_6$ ) and other NMVOCs outside of deep convection regions is distinctly secondary. NMVOCs are subject to the same convective transport as  $NO_x$  and PAN formation occurs where both have the highest values. The lifetime of  $NO_x$  is short throughout the troposphere which implies that PAN production in the UT can be associated with deep convection. There is also a contribution to PAN production from stratospheric air penetrating into the troposphere (Liang et al., 2011). Tropopause folding is a significant source of exchange between the stratosphere and the troposphere (Gettelman et al., 2011). This is an extratropical process that likely contributes to the PAN formation maxima over North America, Europe and Asia shown in Figure 1(a) via enhanced conversion of ethane. In the model it is unable to obscure the relationship between PAN formation and  $NO_x$  pollution source regions.

### **3. Comparison of model simulations with observations**

#### **3.1 Comparison with aircraft measurements**

Figure 2 shows scatter plot between aircraft observations and model simulations at the coherent locations. Both aircraft observations and model simulations are averaged for the monsoon season and altitude ranges. It indicates that model simulated PAN,  $O_3$  and  $NO_x$  show good agreement with aircraft measurements, correlation coefficient >0.7 and significance (P-value) varies between 0.00 to 0.3 indicating correlation is significant at 95% confidence level. However simulated  $HNO_3$  between 2 - 6 km and 6 -10 km does not agree well with aircraft observations. A point to point comparison of (latitude-longitude transects at various altitudes) simulated PAN,  $NO_x$ ,  $O_3$  and  $HNO_3$  (for the period 1995-2005) with aircraft observations are presented by

Fadnavis et al. (2014). These plots show good agreement between model simulations and aircraft observations. Vertical variation of simulated ozone also shows good agreement with ozonesonde measurements over India (see supplementary figure S3 in Fadnavis 2014). It should be noted that current model simulations (2000-2010) show better agreement with aircraft observations than Fadnavis et al., (2014). Figures showing the difference between these simulations and the aircraft observations are provided in the supplement as Figure S2. The model bias varies with species and altitude. In general, the bias in PAN is ranging from -20 ppt to 80 ppt, for ozone from -2ppb to 40 ppb, for HNO<sub>3</sub> from -20ppt to 75 ppt while NO<sub>x</sub> mixing ratios show a good agreement with CAIPEEX measurements over the Indian region. Unfortunately, there were no measurements of PAN or HNO<sub>3</sub> made during CAIPEEX.

### 3.2 Comparison with MIPAS-E retrievals

In order to study the influence of monsoon circulation on the distribution of PAN in the UTLS region, multi-year averages (2005-2011) of seasonal mean (June-September) PAN retrievals from MIPAS-E are analyzed. Figure 3 (a) presents these data for the altitude range 14 - 16 km, and Figure 3 (b) shows the corresponding ECHAM5-HAMMOZ results for comparison. MIPAS-E observations show maximum PAN mixing ratios (~200 - 230 ppt) over (1) the Asian monsoon anticyclone region (12° - 40° N, 20° - 120° E), and (2) over parts of North America, the Gulf Stream, (3) southern Atlantic Ocean and west coast of tropical Africa. ECHAM5-HAMMOZ CTRL simulations also show high PAN concentration at these locations, however PAN concentrations are lower than MIPAS-E observations and appear somewhat more localized. MIPAS-E exhibits a PAN maximum originating from African sources over the South Atlantic, whereas the model shows this maximum over the African continent. This may be the outflow of

biomass burning over central and southern Africa during summer monsoon, which might be underestimated in the model. The biomass burning region of Africa during the ASM season is  $\sim 30^{\circ}\text{S} - 20^{\circ}\text{N}$ ;  $20^{\circ}\text{W} - 30^{\circ}\text{E}$  (Glanter et al., 2000). The longitude-altitude and latitude-altitude cross-sections of MIPAS-E observed and simulated PAN over the biomass burning region are plotted in figure S3. Model simulation shows that the biomass plume rising from Africa move westward and northward over the Atlantic Ocean and merges with South American plume. From satellite, aircraft observations and model simulations Real et al., (2010), and Barret et al., (2008) reported a plume in the mid and Upper Troposphere (UT) over the southern Atlantic which originates from central African biomass burning fires.

The difference between ECHAM5-HAMMOZ simulation and MIPAS observations **are shown** in figures S3 (c) and S3 (f). These figures show that the model underestimates biomass burning PAN by 20 - 60 ppt. These differences may also be related to issues in the vertical transport of PAN, or to a possible **underestimation** of the emission sources of NMVOCs. Uncertainties in the rate coefficients and absorption cross sections of PAN may also play a role. Furthermore, anthropogenic  $\text{NO}_x$  emissions are mostly underestimated in the emission inventories (Miyazaki et al., 2012). As discussed in Fadnavis et al. (2014), UTLS PAN over the ASM is sensitive to  $\text{NO}_x$  emission changes in India or China. In their study, also performed with ECHAM5-HAMMOZ, a 73 %  $\text{NO}_x$  emission change in India lead to a PAN increase of 10 - 18 %, while a 73 %  $\text{NO}_x$  emission change in China changed PAN over the ASM by 18 - 30 %. The cross-section plots of (see figure S4) differences in MIPAS-E PAN with model simulated PAN indicate that in the UTLS, MIPAS-E PAN is higher than model simulated PAN by  $\sim 20 - 60$  ppt (except **at** 20 km). **PAN** is lower by 20 - 40 ppt over eastern part of **ASM** anticyclone (Southern India and South East Asia) and also over Indonesia and northern Australia. In general, in the



ASM region, during the monsoon season, MIPAS-E PAN is higher than model by 30 - 60 ppt between 8 - 16 km and the difference between MIPAS-E and model PAN vary between +40 ppt to -40 ppt between 17 and 20 km.

#### **4. Transport of PAN during monsoon season**

##### **4.1 Transport from Northern tropical land mass**

Figure 3(a) shows high concentrations of MIPAS-E PAN at 14-16 km over Asia, North America and tropical Africa. ECHAM5-HAMMOZ simulations (figure 3b) also show similar distribution. This may be due to transport from boundary layer into the UTLS by the monsoon convection from respective regions. ECHAM5-HAMMOZ simulated OLR and 850hpa winds averaged for the monsoon season are shown in Figure S5(a). They indicate the extent of deep convection near the surface. NECP reanalysis OLR and 850 hPa winds averaged for monsoon season (2000-2010) are plotted in figure S5 (b) for comparison. These figures indicate that the model can reproduce deep convection as well as the large scale circulation. Cross-section of distribution of simulated Cloud Droplet Number Concentration (CDNC) and ice crystal number concentration (ICNC) over Asia, North America and tropical Africa confirms strong convective transport from these regions (figure S5 (c)-(e)). It should be noted that vertical velocities in a large scale model also indicate rapid uplift in deep convective regions. From satellite observations and model simulations Park et al., (2009) reported transport of fraction of boundary layer carbon monoxide (CO) into the UTLS by the Asian monsoon convection.

To illustrate vertical transport, longitude-altitude cross sections of PAN mixing ratios averaged over the region  $0^{\circ}$  -  $30^{\circ}$  N for June-September as obtained from MIPAS-E and

ECHAM5-HAMMOZ are shown in Figures 4(a) and (b) respectively. Both MIPAS-E observations and ECHAM5-HAMMOZ simulations show elevated levels of PAN (200 - 250 ppt) near  $80^{\circ}$  E -  $100^{\circ}$  E (ASM),  $30^{\circ}$  W -  $30^{\circ}$  E (WAM) and  $80^{\circ}$  W -  $100^{\circ}$  W (NAM) region. The simulated PAN distribution along with winds plotted in Figure 4(b) show cross tropopause transport from these regions. It reveals that transport of boundary layer PAN to the UTLS mainly occurs from strong convective regions, i.e. Bay of Bengal ( $\sim 80^{\circ}$  E -  $90^{\circ}$  E), South China Sea ( $\sim 100^{\circ}$  E -  $120^{\circ}$  E), western Atlantic Ocean (Gulf Stream region) and Gulf of Mexico ( $80^{\circ}$  W -  $100^{\circ}$  W). MIPAS-E observations and model simulations show that the transport due to ASM is strongest and reaches deepest into the lower stratosphere. This is due to the more intense deep convection activity over the ASM region compared to the NAM region (see figure S5 (c)-(e)). Figure 4(c) presents the differences between MIPAS and model simulated PAN. It appears that the model PAN is overestimated over the ASM (20 - 30 ppt) and underestimated over the NAM (50 - 70 ppt) and WAM (20 - 50 ppt) regions between 8km and 18km. However, the overestimation in the UT in the ASM is difficult to explain on physical grounds and is more likely to be a MIPAS-E sampling issue as discussed later.

## 4.2 Transport from southern tropical land mass

In order to understand transport of PAN due to southern WAM, SAM and AUSM, we show longitude-pressure sections of MIPAS-E observations and model simulated PAN concentrations averaged over  $0^{\circ}$  -  $25^{\circ}$  S in Figure 4(d)-(e) respectively. The model has plumes near  $20^{\circ}$  E,  $100^{\circ}$  E and  $80^{\circ}$  W. These three regions of convective transport are (1) tropical southern Africa  $10^{\circ}$  -  $40^{\circ}$  E, referred to as South Africa, (2) Indonesia and northern parts of Australia  $\sim 100^{\circ}$  -  $110^{\circ}$  E and (3) South America  $\sim 70^{\circ}$  -  $80^{\circ}$  W. Outflow from Indonesia and from northern parts of Australia

403 (~100° E) penetrates deep into the UTLS. Tropical Rainfall Measuring Mission (TRMM)  
404 satellite observations show high frequency of intense overshooting convection over these areas  
405 (during the monsoon season) with highest density in the belt 0° - 10° S over the Caribbean,  
406 Amazon, Congo and Southern Maritime Continent (Liu and Zipser, 2005). The analyses of  
407 vertical winds show strong transport from 10° - 40° E, 100° - 110° E, 70° - 80° W (in the belt 0° -  
408 10° S) (figure not shown). The amount of high level cloud fraction is also high over these  
409 regions. Distribution of CDNC and ICNC show deep convection over these regions (Figure not  
410 shown). The model simulations show high PAN concentrations reaching the UTLS. Thus  
411 transport due to deep convection is reasonably well captured by the model. However, the  
412 MIPAS-E retrievals only show a plume rising over South Africa and no enhancement over the  
413 AUSM (Indonesia-Australia) and SAM regions. Figure 4(e) shows that the plumes from the three  
414 outflow regions are mixed in the UT (8 - 14 km) by the prevailing westerly winds. The reasons  
415 for a single plume seen in MIPAS-E may be that lower concentrations of PAN reach these  
416 altitudes (above 8 km) from SAM and AUSM and mix with the plume over South Africa. There  
417 are indications of elevated PAN concentrations at the lower boundary in Figure 4 (d).  
418 Simulations show lower PAN mixing ratios over the longitudes of SAM and AUSM (see figure  
419 4(e)). The differences between MIPAS observations and simulations (figure 4(f)) show that  
420 model PAN is overestimated in the AUSM (10-30ppt) and is underestimated over the southern  
421 WAM (20 - 70 ppt) and SAM (20 - 50 ppt) between 10 km and 18km. It is likely that the three  
422 plume structure in the UT seen in model is being obscured in the observations due to sampling  
423 issues since periods of deep convection reaching significantly above 8 km are associated with  
424 significant cloud cover.

Figure 4 shows that simulated transport of PAN due to ASM, NAM and WAM convection are stronger and penetrate deeper into the UT compared to SAM and AUSM. This is consistent with the distribution of deep convection noted by Gettelman et al. (2002). In general, the PAN amounts in the UTLS in the model are less than those observed by MIPAS-E. This may be due to an **underestimation** of the chemical PAN source from VOC precursors or too little vertical **transport in the model** or a combination of both. Earlier model studies with ECHAM also exhibited too low concentrations of CO in the upper tropospheric outflow (M. Schultz, unpublished data from the NASA Global Tropospheric Experiment TRACE-P mission).

### **4.3 Transport from Asian Summer Monsoon region**

The ASM anticyclone extends from 60°E to 120°E and 10°N to 40°N (see figure 3 (b)). Latitude-altitude cross sections over the ASM anticyclone (60° E - 120° E) of MIPAS-E observed PAN (plotted in the altitude range 8 - 20 km) and ECHAM5-HAMMOZ CTRL simulations are shown in Figures 5(a) and (b), respectively. ECHAM5-HAMMOZ simulations are similar to MIPAS-E retrievals of PAN. There is indication of plume ascent into the lower stratosphere. The ECHAM5-HAMMOZ simulations also show transport of subtropical boundary layer PAN into the UTLS due to deep convection. This is not visible in the MIPAS-E data because of the lack of data below 8 km. Figure 5 (b) shows that there is transport from 40° - 50° N reaching up to 10 km (~200 hPa). Park et al. (2004, 2007, 2009) and Randel and Park (2006) noted that trace species are introduced into the monsoon anticyclone at its eastern end around 200 hPa. The uplift over south-east Asia and the base of the Himalayas in India pumps tracers into the upper tropical troposphere where they get horizontally redistributed by the anticyclonic circulation and form the region of high PAN values between 40° N and high latitudes. Figure

10(c) shows that the mid-latitude maximum seen in Figure 5(c) is due to pollution transport from Europe. The Chinese emissions are feeding into this large plume over Russia and are transported partly and diluted over the extratropical Pacific Ocean. The latitude-altitude section of differences between MIPAS and simulated PAN indicates that ASM plume is underestimated in the model (see figure 5 (c)). It is interesting to compare figure 4(c) (longitude –altitude section) and figure 5(c) (latitude-altitude section). The reason for underestimation of the ASM plume in the latitude-altitude section may be due to a lower contribution from the eastern part of anticyclone in the model. Figure S4 shows model PAN is underestimated over Southern India and South East Asia in the UT and overestimated in the lower stratosphere.

In order to understand the impact of transport from ASM region on the rest of the world, we analyze **differences** between reference and Asia-10% simulations (reference –Asia-10%). The **latitude-altitude and longitude-altitude** cross sections over the ASM region (Figures 5 (d) and 5(e)) show transport of ~5-20 ppt of PAN into the lower stratosphere. The horizontal cross sections at 14 km to 21 km (figures 5 (f) – 5(i)) show that Asian PAN is transported to northern Atlantic by subtropical westerly winds. **These figures show that a 10% change in Asian emissions (NO<sub>x</sub> and NMVOCs) transports ~5-30 ppt into the UTLS over Asia and 1-7 ppt of PAN in the UTLS of Northern subtropics and mid latitudes.**

#### 4.4 Transport from North American monsoon region

Figures 6(a) and (b) exhibit latitude-altitude sections of PAN from MIPAS-E retrievals and ECHAM5-HAMMOZ simulations (seasonal mean for July-September) over the North American monsoon region between 70° W - 120° W. MIPAS-E observations and the model indicate

transport of PAN into the UTLS. The distribution of ECHAM5-HAMMOZ simulated PAN from the boundary layer to UTLS shows the source region is at around 40° N. There is convective uplift of PAN over the northern Gulf of Mexico region and over the Gulf Stream. High amount of pollutants emitted from north east America from a number of power plants are located in Atlanta, Washington, Chicago, Boston, Jacksonville (CEC report, 2011). The tropospheric NO<sub>2</sub> columns retrieved from the SCIAMACHY and OMI satellite instrument shows high amounts of anthropogenic NO<sub>2</sub> emissions over this region (Lamsal et al., 2011, Miyazaki et al., 2012). The model simulations show high amount of PAN concentrations over this region (see figures 10(a)-(d)). The monsoon convection lifts these pollutants to the UT. The outflow of these pollutants is over the Atlantic (see figures 3 (a)). TRMM precipitation radar observations show significant overshooting convective activity over this region during the monsoon season (Liu and Zipser, 2005). The vertical distribution of differences in MIPAS and simulated PAN shows that PAN is underestimated in the model (see figure 6(c)) over North and South America (10-60 ppt) between 10-18km, however PAN is overestimated in the model between 8-10km in the region near 30°N . As discussed above this may be associated with European emissions and transport.

Figures 6 (d) - 6 (e) show impact of North American emission (reference – North-America-10%) on the transport of PAN. The figure shows cross tropopause transport of PAN by North American monsoon convection. The amount of PAN transported (~1-5 ppt) into the lower stratosphere is less than for the ASM (~10-20 ppt). The latitude-longitude distribution of PAN (figures 6 (f) – 6(i)) shows that the upper tropospheric westerly winds transport ~1-10 ppt of PAN to Atlantic, Europe and North China.

## 4.5 Transport from West African region

Figures 7 (a) - (b) show vertical distributions of PAN over the African region (averaged over  $0^{\circ}$  -  $45^{\circ}$  E). MIPAS-E observations and model simulations indicate a plume that crosses the tropopause and enters the lower stratosphere. The model surface fields (see Figure 7(b)) show that this plume arises from latitudes  $5^{\circ}$ - $20^{\circ}$  S over Africa and that it moves equatorward. It subsequently merges with the ASM plume. A prominent tongue of high PAN values between  $30^{\circ}$  and  $60^{\circ}$  N is captured in model simulations. This feature appears to be related to emissions from Europe being transported towards the equator in the upper subtropical troposphere. However, in the model, emissions from Europe are transported poleward instead of equatorward (Figure 7(b)). There is a region of strong descent in the model between  $30^{\circ}$  N and  $40^{\circ}$  N (see Figure 7(b)) which deforms the PAN isopleths around 12 km around  $30^{\circ}$  N. This feature is not seen in the MIPAS-E retrievals and indicates a disagreement of the model with the transport pattern of the atmosphere in this region. The transport of PAN in the  $10^{\circ}$  -  $20^{\circ}$  S latitude band over the Congo, Angola, Tanzania regions of southern and tropical Africa is not pronounced in the model compared to MIPAS-E observations. This behavior indicates that deep tropical convection is underestimated in the model in this latitude band. The vertical distribution of differences in MIPAS and simulated PAN (figure 7(c)) shows that simulated PAN is underestimated over these regions ( $5^{\circ}$  -  $20^{\circ}$  S and  $20^{\circ}$  -  $40^{\circ}$  N) between 10 km and 18 km. The reason may be related to underestimation of deep tropical convection in the model in this latitude band. Simulated PAN is overestimated between 8km and 12km near the equator.

The reference - Africa-10% simulation (figures 7(d)-7(e)) shows that African PAN is transported up to the tropopause. The cross sections over North and South Africa show

penetration of North African plume into the lower stratosphere (~19km). However, PAN transport into the lower stratosphere (~0.2-0.6 ppt) is comparatively less than Asia or North America. Figures 7 (g) - 7(j) show transport of ~5-50 ppt of PAN in the UT (6-12km) of tropical Africa. There is transport from equatorial Africa to Atlantic and Mexico between 6-8km (figures 7 (g) – 7 (h)) which is then transported to North China by upper tropospheric (12km) westerly winds (see figures 7 (j)).

The model simulated latitude-altitude, longitude-altitude cross sections of  $\text{NO}_x$ , and  $\text{HNO}_3$  over the ASM ( $10^\circ\text{N} - 40^\circ\text{N}$ ,  $60^\circ - 120^\circ\text{E}$ ), NAM ( $10^\circ\text{N} - 40^\circ\text{N}$ ,  $70^\circ\text{W} - 120^\circ\text{W}$ ) and WAM ( $0^\circ - 25^\circ\text{S}$ ,  $0^\circ - 45^\circ\text{E}$ ) are shown in Figures 8 (a) – 8(j), respectively. Figures 8 (a)- 8(e) show transport features of  $\text{NO}_x$ . These are similar to those seen in the distribution of PAN, but with sharper signatures due to the shorter lifetime of  $\text{NO}_x$ . This shows that monsoon convection lifts boundary layer pollutants including  $\text{NO}_y$  species to the UTLS. The distribution of  $\text{HNO}_3$  (see Figures 8 (f) - 8(j)) shows a complex pattern. Comparing Figure 4(b), the region around  $100^\circ\text{E}$  with intense convective uplift corresponds to  $\text{HNO}_3$  depletion from the surface to above 10 km. In fact, the upper tropospheric region of the ASM anticyclone exhibits much lower values of  $\text{HNO}_3$  compared to all the other longitudes in the  $10^\circ - 40^\circ\text{N}$  band (Figure 8(h)). This suggests that in the model the convective transport in the ASM region is associated with efficient removal by wet scavenging. In contrast, the North American monsoon region has  $\text{HNO}_3$  ascending to the UT with significantly less loss. This is likely due to the fact that convection involved in vertical transport during the NAM is not as intense and not as deep as in the case of the ASM and there are differences in wet scavenging. Figure 8(g) shows that the plume rising from South America moves towards the equator but does not have the extension into the UT as the North American plume. These are June-September averages and the ITCZ is on the northern



hemisphere side during this period. Thus, weaker convective transport is to be expected on the southern hemisphere side of the equator during this period. Figure 8 (i) shows significant transport of African emissions around  $\sim 0^{\circ}$  -  $15^{\circ}$  S and a plume rising from Europe ( $\sim 35^{\circ}$  N -  $60^{\circ}$  N) as well.

Figures 9 (a) –9 (f) show vertical distribution of  $\text{HNO}_3$  and  $\text{O}_3$ , over Asia, North America and Africa as obtained from differences between the reference and Asia-10%, reference and North-America-10% as well as reference and Africa-10% simulation. It is evident that transport of  $\text{HNO}_3$  for Asia-10% simulation is deeper in the UT ( $\sim 16\text{km}$ ) than North-America-10% and Africa-10% simulations. It can be seen that Asia-10%, North-America-10% and Africa-10% simulations transport  $\sim 7\text{--}10$  ppt,  $\sim 5\text{--}7$  ppt and  $\sim 3\text{--}5$  ppt of  $\text{HNO}_3$  in the UT of their respective regions.

In the UT, between 6km and 10km, Asia-10% simulation shows transport of  $\sim 10\text{--}15$  ppt of  $\text{HNO}_3$  over Western Pacific and  $\sim 3\text{--}10$  ppt over tropical America by the subtropical westerly winds (figure not included). North-America-10% simulation shows transport of  $\sim 5\text{--}7$  ppt of  $\text{HNO}_3$  over Atlantic, North Africa, Saudi Arabia and North China by the subtropical westerly winds and  $\sim 3\text{--}5$  ppt of  $\text{HNO}_3$  over equatorial pacific, Indonesia, China and India by the tropical easterly winds. Africa-10% simulation shows transport of  $\sim 3\text{--}5$  ppt  $\text{HNO}_3$  from North Africa to North America, equatorial pacific, also there is transport of  $\sim 4$  ppt of  $\text{HNO}_3$  from South Africa to Atlantic, South America, Indonesia, China and India by the tropical easterly winds (figure not included).

North-America-10% simulation shows transport of boundary layer ozone extending up to the tropopause, which are higher than for the Asia-10% and Africa-10% simulations (figures 9

(d) – 9 (f)). Asia-10%, North-America-10% and Africa-10% simulations show transport ~1-2 ppb, ~0.8-1.5 ppb and ~0.4-0.6 ppb of ozone in the UT of their respective regions.

In the UT, between 6km and 10 km, Asia-10% simulation shows transport of ozone ~1.5 ppb to Western Pacific and 0.8 ppb to Mexico and United States by the subtropical westerly winds (figure not included). North-America-10% simulation shows transport of 0.4-1.5 ppb of O<sub>3</sub> to equatorial Pacific extending up to Indonesia by the tropical easterly winds. There is some outflow (~0.6ppb) over Atlantic by the subtropical westerly winds as well (figure not included). Africa-10% simulation shows transport of ~0.4-0.8 ppb of ozone to equatorial Atlantic and Mexico (figure not included).

It can be seen that similar emission change over Asia, North America and Africa causes highest change in HNO<sub>3</sub> and Ozone in the UT over Asia and least over Africa. In the UT, between 6km and 10 km, transport of HNO<sub>3</sub> by Asia-10% (~3-10 ppt of HNO<sub>3</sub> to tropical America) is higher than North-America-10% (~3-7 ppt of HNO<sub>3</sub> to China and India) and Africa-10% (~3-5 ppt of HNO<sub>3</sub> to tropical America, China and India). Similarly ozone transport is higher for Asia-10% than North-America-10% and Africa-10% simulations.

#### **4.6 Horizontal transport**

PAN concentrations from MIPAS-E and ECHAM5-HAMMOZ at different altitudes are analyzed to **investigate** horizontal transport. Figure 10(a) shows the distribution of PAN from ECHAM5-HAMMOZ simulations near the surface (2 km). Sources of PAN are apparent over South America, southern Africa, North America, Europe, Russia and northern China/Mongolia. The PAN distribution at 4 km (see Figure 10(b)) shows high concentrations above these regions indicating vertical transport. Figures 10(c) and 10 (d) show the distribution at 6 km and 8 km.

The upper level anticyclonic circulation between 10° N and 30° S over the Atlantic transports PAN from central Africa towards America and from Brazil towards southern Africa. The large Scale Biosphere-Atmosphere Regional Experiment in Amazonia (LBA-CLAIRE-98) campaign observations (Andreae et al., 2001) and African Monsoon Multidisciplinary Analysis (AMMA) project (Real et al., 2010) show that the biomass burning plume originating from Brazil is lifted to altitudes around 10 km. This plume is entrained into deep convection over the northern Amazon, transported out over the Atlantic and then returned to South America by the circulation around a large upper-level anticyclone. This transport is well captured by the model.

North American pollution is also being transported by the westerly winds over Eurasia, forming an organized belt. This transport pattern persists up to 12 km (Figure 10 (e) and 10(g)). MIPAS-E observations at 12 km also show this transport pattern. The source region for the PAN from southern Africa is the region of active biomass burning. Since this region is located in the tropics, the outflow is over the Atlantic due to the prevailing easterly winds. ECHAM5-HAMMOZ simulations show similar transport (see Figures 10(e)). But there are differences; in particular the transport over tropical Africa does not get displaced over the Atlantic Ocean. As noted above, there are significant transport differences between the model and observations in this longitude band. Another difference is that PAN is not transported westward over Central America and towards the Pacific Ocean.

Figures 10(f)-10(h) show the distribution of PAN from ECHAM5-HAMMOZ simulations and MIPAS-E retrievals, in the lower stratosphere (18 km). In both data sets PAN is transported westwards from ASM, NAM and WAM by prevailing easterly winds and maximizes in the region of the ASM anticyclone.

As can be seen from the above discussions, the ASM, NAM, and WAM outflow and convection over the Gulf Stream play an important role in the transport of boundary layer pollution into the UTLS. Previous studies (e.g. Fadnavis et al., 2013) indicated that over the Asian monsoon region, transport into the lower stratosphere occurs and there is significant vertical transport over the southern slopes of the Himalayas (Fu et al., 2006, Fadnavis et al., 2013) and also over the region spanned by the Bay of Bengal and the South China Sea (Park et al., 2009). Pollutant transport due to North American convection and tropical African outflow does not penetrate as deep into the stratosphere as the ASM. However there is clear indication that in the UT, middle latitude westerly winds connect the North American pollution to the ASM.

Figures 3-7 and figure 10 show that in the UT, westerly winds drive North American and European pollutants eastward to at least partly merge with the ASM plume. Strong ASM convection transports these remote and regional pollutants into the stratosphere. The Caribbean is a secondary source of pollutant transport into the stratosphere. In the stratosphere the injected pollutants are transported westward by easterly winds and into the southern subtropics by the Brewer-Dobson circulation.

## **5.0 Impact of Lightning on tropospheric PAN, NO<sub>x</sub>, HNO<sub>3</sub> and ozone**

In the ASM region and during the monsoon season the NO<sub>x</sub> released from intense lightning activity enhances the formation of PAN, HNO<sub>3</sub> and ozone in the middle and upper troposphere which is already relatively strong due to the intense solar radiation along with high background concentrations of NO<sub>x</sub>, HO<sub>x</sub> and NMVOCs (Tie et al., 2001). PAN, HNO<sub>3</sub> and O<sub>3</sub> produced from

lightning may get transported in the lower stratosphere by deep monsoon convection and contribute to anthropogenic emission transport of these species. In order to understand contribution of lightning and the dominating lightning production regions, we analyze difference between control and light-off simulations. Figure 11(a)-(d) shows the percentage changes in model simulated ozone,  $\text{HNO}_3$ , PAN and  $\text{NO}_x$  due to lightning as zonally averaged spatial distribution of seasonal mean (June-September) mixing ratios. The analysis indicates that the impact of lightning on these species is largest in the tropical UT between  $40^\circ \text{N}$  -  $40^\circ \text{S}$  and between 8 km and 14 km. In the tropical mid troposphere lightning produced maximum ozone is  $\sim 15 - 25 \%$  (12 - 24 ppb),  $\text{HNO}_3 \sim 40 - 60 \%$  (50 - 90 ppt), PAN  $\sim 15 - 25 \%$  (70 - 140 ppt) and  $\text{NO}_x \sim 20 - 40 \%$  (10 - 35 ppt) while in the UT ozone is  $\sim 20 - 30 \%$  (20 - 28 ppb),  $\text{HNO}_3 \sim 60 - 75 \%$  (80 - 110 ppt), PAN  $\sim 28 - 35 \%$  (120 - 170 ppt), and  $\text{NO}_x \sim 50 - 75 \%$  (20 - 65 ppt). Our results are consistent with model simulations by Tie et al., (2001) and Labrador et al. (2005). The spatial distributions of  $\text{NO}_x$ , ozone, PAN and  $\text{HNO}_3$  produced from lightning (see figures 12 (e) - (h)) indicate that in the UT (12 km) increases in  $\text{O}_3 \sim 20 - 25 \%$  (11 - 17 ppbv),  $\text{HNO}_3 \sim 40 - 70 \%$ , PAN  $\sim 25 - 35 \%$  and  $\text{NO}_x \sim 55 - 75 \%$ , over North America are in agreement with previous studies (e.g Labrador et al., 2005; Hudman et al. 2007; Zhao et al., 2009; Cooper et al., 2009), over equatorial Africa (PAN 30 - 45 %,  $\text{HNO}_3 \sim 70 - 80 \%$ ,  $\text{O}_3 \sim 25 \%$ ,  $\text{NO}_x \sim 70 \%$ ) agrees well with Barret et al., 2010; Bouarar et al., 2011 and over the ASM region (PAN  $\sim 25 \%$ ,  $\text{HNO}_3 \sim 65 - 70 \%$ ,  $\text{O}_3 \sim 20 \%$ ,  $\text{NO}_x \sim 60 - 70 \%$ ) agrees with Tie et al., (2001). These regions coincide with regions of convective vertical transport of PAN (as seen in figures 4 and 5). Lightning produced PAN will be lifted into the lower stratosphere by the monsoon convection along with anthropogenic emissions and will redistribute in the tropical lower stratosphere. Latitude-longitude cross sections of lightning induced PAN,  $\text{NO}_x$ , ozone and  $\text{HNO}_3$  formation at altitudes

648 between 8 - 14 km show that the production of PAN, NO<sub>x</sub>, ozone and HNO<sub>3</sub> is less over the  
649 ASM region than over the equatorial Americas and Africa (also seen in figure 11). The high  
650 amounts of PAN over the ASM are therefore primarily due to anthropogenic emission transport  
651 into the UTLS from the source regions in Southern and Eastern Asia. As discussed in Fadnavis  
652 et al., 2014, NO<sub>x</sub> emissions are estimated to have changed by 38 % in India and 76 % in China,  
653 respectively during 2002 - 2011 period. From sensitivity simulations they deduced corresponding  
654 changes in upper tropospheric PAN are > 40 %, O<sub>3</sub> by > 25 % and HNO<sub>3</sub> by > 70 % over the  
655 Asian monsoon region. These effects are larger than the impact of lightning NO<sub>x</sub> emissions over  
656 this region (figure 11 (e)-(h)).

657

## 6. Conclusions

In this study statistical analysis of simulated and satellite-retrieved mixing ratios of PAN, NO<sub>x</sub>, and HNO<sub>3</sub> is presented in order to determine the transport patterns of pollution into the Asian monsoon region and the impact of pollution flowing out of the ASM into other regions of the global atmosphere. The analysis focused on the upper troposphere and lower stratosphere and covered the period 2002 - 2011. In ECHAM5-HAMMOZ simulations both NO<sub>x</sub> and NMVOCs emission were simultaneously reduced by 10% over ASM, NAM and WAM to understand transport pathways and their relative contribution the UTLS. As discussed in Fadnavis et al. (2014), NO<sub>x</sub> emissions are estimated to have changed by 38 % in India and 76 % in China, respectively during this period. From sensitivity simulations they deduced corresponding changes in upper tropospheric PAN > 40 %, O<sub>3</sub> by > 2 5% and HNO<sub>3</sub> by > 70 % over the ASM region. These effects are larger than the impact of lightning NO<sub>x</sub> emissions over this region discussed in section 3 of this study.

Interestingly, the ECHAM5-HAMMOZ reference simulation reveals that in the UT, westerly winds drive North American and northward propagating South African pollutants eastward where they mix with the ASM plume. Deep convection and strong diabatic upwelling in the ASM, convectively transports a part of these plumes into the lower stratosphere. The Caribbean region is another source of pollution transport into the stratosphere. Some cross tropopause transport occurs due to convection over North America and Southern Africa as well. In the lower stratosphere the injected pollutants from ASM, WAM and NAM are transported westward by easterly winds and into the southern hemisphere subtropics by the Brewer-Dobson circulation. The emission sensitivity simulations Asia-10%, North-America-10% and Africa 10%

confirm these transport pathways. In the southern hemisphere, plumes rising from convective zones of South Africa, South America and Indonesia-Australia are evident in the model simulations, but are not seen in the MIPAS retrievals. PAN concentrations are higher in the plume rising from South Africa than SAM and AUSM. In the UT, they merge by the prevailing westerly winds. MIPAS-E observations in the UTLS show a single plume over South Africa and no enhancement over SAM or AUSM. The reasons for the single plume seen in MIPAS-E may be that although there is uplifting by each of the three monsoon systems lower concentrations of PAN reach these altitudes (above 8 km) from SAM and AUSM until they merge with South African plume. It is also possible that the three plume structure in the UT seen in the model is being obscured in the observations due to sampling issues. Convective cloud cover is strongly associated with deep convection in the ASM region. The MIPAS-E data has a PAN minimum in the UT right in the longitude band of the deep convection over the southern flanks of the Himalayas (Figure 4(a)). This feature is unphysical and clearly identifies a sampling bias. However, the model is also not fully reproducing the latitudinal structure of the PAN in the ASM region UTLS which indicates that there are differences in both the distribution of convection and the large scale circulation.

The horizontal transport of PAN analyzed from ECHAM5–HAMMOZ simulations show that the PAN from southern Africa and Brazil is transported towards America by the circulation around a large upper-level anticyclone and then lifted to the UTLS in the NAM region. This is also evident in the Africa-10% simulation.

The vertical distribution of simulated  $\text{HNO}_3$  over the monsoon regimes shows low concentrations above 10 km at the foothills of the Himalayas. In contrast, the results show strong



uplifting of  $\text{HNO}_3$  into the UT with NAM convection. This may be due to the fact that NAM convection is not as intense as the ASM and there may be more wet removal of nitrogen oxides in the ASM convection. The model simulations indicate a higher efficiency of  $\text{NO}_x$  conversion to  $\text{HNO}_3$  over the Indian region compared to NAM.

The change in emission (both  $\text{NO}_x$  and NMVOCs emissions were simultaneously reduced by 10%) over each of ASM, WAM and NAM regions show that Asia-10% transport ~5-30 ppt of PAN in the UTLS over Asia and ~1-10 ppt in the UTLS Northern subtropics and mid latitude. North-America-10% simulation shows transport of ~1-5 ppt of PAN over Atlantic, Europe and North China (between 12-14km) and 0.4-3ppt over Asia (near 16km). Africa-10% simulation shows transport from equatorial Africa to Atlantic and North America between 6 – 8 km, which is then transported to Asia by upper tropospheric westerly winds (near 12km).

Transport of  $\text{HNO}_3$  is deeper in the UT (~16km) in Asia-10% simulation than North-America-10% and Africa-10% simulations. Asia-10%, North-America-10%, Africa-10% simulations show transport of ozone ~1-2 ppt, 0.8-1.5 ppt and 0.4-0.6 ppt in the UT over respective regions.

In the UT between 6km and 10km, transport of  $\text{HNO}_3$  by Asia-10% (~3-10 ppt of  $\text{HNO}_3$  to tropical America) is higher than North-America-10% (transport of 3-7 ppt of  $\text{HNO}_3$  to China and India) and Africa-10% (~3-5 ppt of  $\text{HNO}_3$  to tropical America, China and India) simulations. Similarly transport of ozone is higher for Asia-10% than North-America-10% and Africa-10% simulations. Comparison of emission change over Asia, North America and Africa shows highest transport of  $\text{HNO}_3$  and ozone in the UT over Asia and least over Africa.

Lightning production of  $\text{NO}_x$  may enhance PAN concentrations in the UT and affect its transport into the lower stratosphere. The percentage change in lightning produced ozone,  $\text{HNO}_3$ , PAN and  $\text{NO}_x$  has been evaluated with a sensitivity simulation. In the UT, lightning causes significant increases in these species over equatorial America, equatorial Africa and the ASM region. These regions coincide with intense convective zones with significant vertical transport. Lightning production is higher over equatorial Africa and America compared to the ASM. However, the vertical distribution shows that higher amounts of PAN are transported into the UT in the ASM region. This indicates that the contribution of anthropogenic emission to PAN in the UTLS over the ASM, is higher than that of lightning. This is consistent with the fact that anthropogenic emissions in the ASM region are higher than in the NAM and WAM (Lamsal et al., 2011, Miyazak et al., 2012).

*Acknowledgements:* The authors thank the MIPAS-E teams for providing data and the High Power Computing Centre (HPC) in IITM, Pune, India, for providing computer resources. Authors are also thankful to anonymous reviewers and the Editor for their valuable suggestions.

## References

- Andreae, M. O., Artaxo, P., Fischer, H., Freitas, S. R., Grégoire, J.-M., Hansel, A., Hoor, P., Kormann, R., Krejci, R., Lange, L., Lelieveld, J., Lindinger, W., Longo, K., Peters, W., de Reus, M., Scheeren, B., Silva Dias, M. A. F., Ström, J., Velthoven, P. F. J. van and William, J.: Transport of biomass burning smoke to the upper troposphere by deep convection in the equatorial region, *Geophys. Res. Lett.*, 28, 951-958, 2001.
- Arnold F. & Hauck G., Lower stratosphere trace gas detection using aircraft-borne active chemical ionization mass spectrometry, *Nature*, 315, 307-309, |doi:10.1038/315307a0, 19 December 1984.
- Aumann, H. H. and Ruzmaikin, A.: Frequency of deep convective clouds in the tropical zone from 10 years of AIRS data, *Atmos. Chem. Phys.*, 13, 10795–10806, 2013.
- Barret, B., Williams, J. E., Bouarar, I., Yang, X., Josse, B., Law, K., Pham, M., Flochmoen, E. Le, Liousse, C., Peuch, V.H., Calver, G.D., Pyle, J.A., Sauvage, B., Velthoven P. van and Schlager, H.: Impact of West African Monsoon convective transport and lightning NO<sub>x</sub> production upon the upper tropospheric composition: a multi-model study, *Atm. Chem. Phys.*, **10**, 5719-5738, doi:10.5194/acp-10-5719-2010, 2010.
- Barret B., Ricaud P., Mari C., Attie´ J.-L., Bousserez N., Josse B., Flochmoen E. LeLivesey N. J., Massart S., Peuch V.-H., Piacentini A., Sauvage B., Thouret V., and Cammas J.-P. Transport pathways of CO in the African upper troposphere during the monsoon season: a study based upon the assimilation of spaceborne observations, *Atmos. Chem. Phys.*, 8, 3231–3246, 2008.

761 Barth, M., Lee, C. J., Hodzic, A. Pfister, G., Skamarock, W. C., Worden, J. , Wong, J., and  
 762 Noone, D.: Thunderstorms and upper troposphere chemistry during the early stages of the  
 763 2006 North American Monsoon, *Atmos. Chem. Phys.*, 12, 11003–11026, 2012.

764 Bouarar, I., Law, K. S., Pham, M., Lioussé, C., Schlager, H., Hamburger, T., Reeves, C. E.,  
 765 Cammas, J.-P., Ned' el' ec' P., Szopa, S., Ravagnani, F., Viciani, S., D'Amato F.,  
 766 Ulanovsky A., and Richter A.: Emission sources contributing to tropospheric ozone over  
 767 Equatorial Africa during the summer monsoon, *Atmos. Chem. Phys.*, 11, 13395–13419,  
 768 doi:10.5194/acp-11-13395-2011, 2011.

769 Carmichael, G. R., Tang Y., Kurata G., Uno I., Streets D., Woo J.-H.,  
 770 Huang H., Yienger J., Lefer B., Shetter R., Blake D., Atlas E., Fried  
 771 A., Apel E., Eisele F., Cantrell C., Avery M., Barrick J., Sachse G.,  
 772 Brune W., Sandholm S., Kondo Y., Singh H., Talbot R., Bandy A.,  
 773 Thorton D., Clarke A., and Heikes B., Regional-scale chemical  
 774 transport modeling in support of the analysis of observations obtained  
 775 during the TRACE-P experiment, *J. Geophys. Res.*, 108(D21), 8823,  
 776 doi:10.1029/2002JD003117, 2003.

777 CEC (Commission for Environmental Cooperation) report on North American Power Plant Air  
 778 Emissions, IBSN : 978-2-89700-008-0, October 2011.

779 Chang, Chih-Pei, Ding Y., Lau, Gabriel Ngar-Cheung, Johnson, R. H, Wang, B., and Yasunari,  
 780 T.: *The Global Monsoon System: Research and Forecast (2nd Edition)* edited by Chih-  
 781 Pei Chang et al., World Scientific Publishing Co, 2011.

782 Choi, Y., Kim, J., Eldering, A., Osterman, G., Yung, Y. L., Gu, Y., and Liou, K. N.: Lightning  
 783 and anthropogenic NO<sub>x</sub> sources over the United States and the western North Atlantic

784 Ocean: impact on OLR and radiative effects, *Geophys. Res. Lett.*, 36, L17806,  
785 doi:10.1029/2009GL039381, 2009.

786 Collier J.C. and Zhang G.J.: Simulation of the North American Monsoon by the NCAR CCM3  
787 and Its Sensitivity to Convection Parameterization, *J. of Clim.*, 2851-2866, 2006.

788 Cooper, O. R., Eckhardt, S., Crawford, J. H., Brown, C. C., Cohen, R. C., Bertram, T. H.,  
789 Wooldridge, P., Perring, A., Brune, W.H., Ren, X., Brunner, D., and Baughcum, S. L.:  
790 Summertime buildup and decay of lightning NO<sub>x</sub> and aged thunderstorm outflow above  
791 North America, *J. Geophys. Res.*, 114, D01101, doi:10.1029/2008JD010293, 2009.

792 Dickerson, R. R., Huffman, G. J., Luke, W. T., Nunnermacker, L. J., Pickering, K. E. , Leslie,  
793 A., Lindsey, C., Slinn, W., Kelly, T., Daum, P., Delany, A., Grennberg, J., Zimmerman,  
794 P., Boatman, J., Ray, J., and Stedman, D.: Thunderstorms: An important mechanism in  
795 the transport of air pollutants, *Science*, 235, 460 – 465, 1987.

796 Dong, L. and Colucci, S. J. : The Role of Deformation and Potential Vorticity in Southern  
797 Hemisphere Blocking Onsets, *J. Atmos. Sci.*, 62, 4043-4056, 2005.

798 Drummond, J. W., D. H. Ehhalt, and A. Volz, Measurements of nitric oxide between 0 – 12  
799 km altitude and 67° N-60° S latitude obtained during STRATOZ III, *J. Geophys. Res.*,  
800 93, 15,831 – 15,849, 1988.

801 Emmons, L. K., Hauglustaine, D. A., Muller, J.-F., Carroll, M. A., Brasseur, G. P., Brunner, D.,  
802 Staehelin, J., Thouret, V., and Marenco, A.: Data composites of tropospheric ozone and  
803 its precursors from aircraft measurements, *J. Geophys. Res.*, 105, 20,497 – 20,538, 2000.

804 Evett, R. R., Mohrle C. R., Hall B. L., Brownb T. J. and Stephens S. L.: The effect of monsoonal  
805 atmospheric moisture on lightning fire ignitions in southwestern North America,  
806 *Agricultural and forest meteorology*, 148, 1478–1487, 2008.

807 Fadnavis, S., Semeniuk, K., Pozzoli, L., Schultz, M. G., Ghude, S. D., Das, S. and Kakatkar, R.:  
808 Transport of aerosols into the UTLS and their impact on the Asian monsoon region as  
809 seen in a global model simulation, *Atmos. Chem. Phys.*, 13, 8771–8786, 2013,  
810 doi:10.5194/acp-13-8771-2013.Fadnavis S, Schultz M. G., Semeniuk K., Mahajan A. S.,  
811 Pozzoli L., Sonbawne S., Ghude S. D., Kiefer M., and Eckert E., Trends in Peroxyacetyl  
812 Nitrate (PAN) in the Upper Troposphere and Lower Stratosphere over Southern Asia  
813 during the summer monsoon season: Regional Impacts, *Atmos. Chem. Phys.*, 14, 12725–  
814 12743, doi:10.5194/acp-14-12725-2014, 2014.

815 Fiore, A. M., Horowitz, L. W., Purves, D. W., Levy II, H., Evans, M. J., Wang, Y., Li, Q., and  
816 Yantosca, R. M.: Evaluating the contribution of changes in isoprene emissions to surface  
817 ozone trends over the eastern United States, *J. Geophys. Res.*, 110, D12303,  
818 doi:10.1029/2004JD005485, 2005.

819 Fischer E. V., Jacob D. J., Yantosca R. M., Sulprizio M. P., Millet D. B., Mao J., Paulot F.,  
820 Singh H. B., Roiger A., Ries L., Talbot R.W., Dzepina K., and Pandey Deolal S.,  
821 Atmospheric peroxyacetyl nitrate (PAN): a global budget and source attribution, *Atmos.*  
822 *Chem. Phys.*, 14, 2679–2698, doi:10.5194/acp-14-2679-2014, 2014.

823 Fischer, H. and Oelhaf, H.: Remote sensing of vertical profiles of atmospheric trace constituents  
824 with MIPAS limb-emission spectrometers, *Appl. Optics*, 35, 2787–2796, 1996.

825 Fischer, H., Birk, M., Blom, C., Carli, B., Carlotti, M., von Clarmann, T., Delbouille, L., Dudhia,  
826 A., Ehhalt, D., Endemann, M., Flaud, J. M., Gessner, R., Kleinert, A., Koopman, R.,  
827 Langen, J., Lopez-Puertas, M., Mosner, P., Nett, H., Oelhaf, H., Perron, G., Remedios, J.,  
828 Ridolfi, M., Stiller, G., and Zander, R.: MIPAS: an instrument for atmospheric and  
829 climate research, *Atmos. Chem. Phys.*, 8, 2151–2188, 2008, doi:10.5194/acp-8-2151-  
830 2008.

831 Fu, R., Hu, Y., Wright, J. S., Jiang, J. H., Dickinson, R. E., Chen, M., Filipiak, M., Read, W. G.,  
 832 Waters, J.W. and Wu, D. L.: Short circuit of water vapour and polluted air to the global  
 833 stratosphere by convective transport over the Tibetan Plateau, *Proc Natl Acad Sci U S A*.  
 834 Apr 11, 103(15), 5664-9, Epub Apr 3, 2006.

835 Galanter, M., H. Levy II, and G. R. Carmichael (2000), Impacts of biomass burning on  
 836 tropospheric CO, NO<sub>x</sub>, and O<sub>3</sub>, *J. Geophys. Res.*, 105(D5), 6633–6653,  
 837 doi:10.1029/1999JD901113.

838 Ganzeveld, L., and Lelieveld, J.: Dry deposition parameterization in a chemistry general  
 839 circulation model and its influence on the distribution of reactive trace gases, *J. Geophys.*  
 840 *Res.*, 100(D10), 20999–21012, doi:10.1029/95JD02266, 1995.

841 Garny, H., and Randel, W. J.: Dynamic variability of the Asian monsoon anticyclone observed in  
 842 potential vorticity and correlations with tracer distributions, *J. Geophys. Res. Atmos.*,  
 843 118, 13,421–13,433, doi:10.1002/2013JD020908, 2013.

844 Gettelman, A., Salby, M. L., and Sassi, F.: Distribution and influence of convection in the  
 845 tropical tropopause region, *J. Geophys. Res.*, 107(D10), 4080,  
 846 doi:10.1029/2001JD001048, 2002.

847 Gettelman, A., Hoor, P., Pan, L. L., Randel, W. J., Hegglin, M. I., and Birner, T.: The  
 848 extratropical upper troposphere and lower stratosphere, *Rev. Geophys.*, 49, RG3003,  
 849 doi:10.1029/2011RG000355, 2011.

850 Glatthor, N., Clarmann, T. von, Fischer, H., Funke, B., Grabowski, U., Höpfner, M., Kellmann,  
 851 S., Kiefer, M., Linden, A., Milz M., Steck, T., and Stiller, G.P.: Global peroxyacetyl  
 852 nitrate (PAN) retrieval in the upper troposphere from limb emission spectra of the  
 853 Michelson Interferometer for Passive Atmospheric Sounding (MIPAS), *Atmos. Chem.*  
 854 *Phys.*, 7, 2775-2787, [www.atmos-chem-phys.net/7/2775/2007/](http://www.atmos-chem-phys.net/7/2775/2007/) doi:10.5194/acp-7-2775-  
 855 2007, 2007.

856 Grewe, V., Brunner, D., Dameris, M. , Grenfell, J.L., Hein, R., Shindell, D. and Staehelin, J. :  
857 Origin and Variability of Upper Tropospheric Nitrogen Oxides and Ozone at Northern  
858 Mid-Latitudes. *Atmos. Environ.*, 35, 3421-3433, 2001.

859 Harris, R. C., et al., The Amazon boundary layer experiment (ABLE 2A) dry season 1985, *J.*  
860 *Geophys. Res.*, 93, 1351-1360, 1988.

861 Harriss, R.C., S.C. Wofsy, D.S. Bartlett, M.C. Shipham, D.J. Jacob, J.M. Hoell, Jr., R.J.  
862 Bendura, J.W. Drewry, R.J. McNeal, R.L. Navarro, R.N. Gidge, and V.E. Rabine, The  
863 Arctic Boundary Layer Expedition (ABLE 3A): July-August 1988, *J. Geophys. Res.*, 97,  
864 16,383-16,394, 1992.

865 Harriss, R.C., S.C. Wofsy, J.M. Hoell, Jr., R.J. Bendura, J.W. Drewry, R.J. McNeal, D. Pierce,  
866 V.Rabine, and R.L. Snell, The Arctic Boundary Layer Expedition (ABLE-3B): July-  
867 August 1990, *J. Geophys. Res.*, 99, 1635-1643, 1994.

868 Hassim, M. E. E., Lane, T. P., and May, P. T.: Ground-based observations of overshooting  
869 convection during the Tropical Warm Pool-International Cloud Experiment, *J. Geophys.*  
870 *Res. Atmos.*, 119, 880–905, doi:10.1002/2013JD020673, 2014.

871 Hoell, J. M., Jr., D. L. Albritton, G. L. Gregory, R. J. McNeal, S. M. Beck, R. J. Bendura, and J.  
872 W. Drewry, Operational overview of NASA GTE/CITE 2 airborne  
873 instrument intercomparisons: Nitrogen dioxide, nitric acid, and peroxyacetyl nitrate, *J.*  
874 *Geophys. Res.*, 95, 10,047-10,054, 1990.

875 Hoell, J. M., Jr., D. L. Albritton, G. L. Gregory, R. L. McNeal, S. M. Beck, R. J. Bendura, and J,  
876 W. Drewry, Operational overview of NASA GTE/CITE-2 airborne instrument  
877 intercomparison: Nitrogen dioxide, nitric acid, and peroxyacetyl nitrate. *J. Geophys.*  
878 *Res.*, 95, 10,047-10,054, 1990

879 Horowitz, L. W., Walters, S., Mauzerall, D. L., Emmons, L. K., Rasch, P. J., Granier, C., Tie, X.,  
880 Lamarque, J., Schultz, M. G., Tyndall, G. S., Orlando, J. J. and Brasseur, G. P.: A global  
881 simulation of tropospheric ozone and related tracers, Description and evaluation of  
882 MOZART, version 2, *J. Geophys. Res.*, 108(D24), 2003.



883 Hudman, R. C., Jacob, D. J., Cooper, O. R., Evans, M. J., Heald, C. L., Park, R. J., Fehsenfeld,  
 884 F., Flocke, F., Holloway, J., Hübler, G., Kita, K., Koike, M., Kondo, Y., Neuman, A.,  
 885 Nowak, J., Oltmans, S., Parrish, D., Roberts, J. M., and Ryerson, T.: Ozone production in  
 886 transpacific Asian pollution plumes and implications for ozone air quality in California, J.  
 887 Geophys. Res., 109, D23S10, doi:10.1029/2004jd004974, 2004.

888 Hudman, R. C., Jacob, D. J., Turquety, S., Leibensperger, E. M., Murray, L. T., Wu, S.,  
 889 Gilliland, A. B., Avery, M., Bertram, T. H., Brune, W., Cohen, R. C., Dibb, J. E., Flocke,  
 890 F. M., Fried, A., Holloway, J., Neuman, J. A., Orville, R., Perring, A., Ren, X., Ryerson,  
 891 T. B., Sachse, G. W., Singh, H. B., Swanson, A., and Wooldridge, P. J.: Surface and  
 892 lightning sources of nitrogen oxides over the United States: magnitudes, chemical  
 893 evolution, and outflow, J. Geophys. Res., 112, D12S05, doi:10.1029/2006JD007912,  
 894 2007.

895 Keim, C., Liu, G. Y., Blom, C.E., Fischer, H., Gulde, T., Höpfner, M., Piesch, C., Ravegnani,  
 896 F., Roiger, A., Schlager, H., and Sitnikov, N.: Vertical profile of peroxyacetyl nitrate (PAN)  
 897 from MIPAS-STR measurements over Brazil in February 2005 and its contribution to  
 898 tropical UT NO<sub>y</sub> partitioning, Atmos. Chem. Phys., 8, 4891-4902, doi:10.5194/acp-8-4891-  
 899 2008, 2008.

900 Khaykin S., Pommereau, J.-P., Korshunov, L., Yushkov, V., Nielsen, J., Larsen, N.,  
 901 Christensen, T., Garnier, A., Lukyanov, A., and Williams, E.: Hydration of the lower  
 902 stratosphere by ice crystal geysers over land convective systems, Atmos. Chem. Phys., 9,  
 903 2275–2287, 2009.

904 Kulkarni J.R., Maheshkumar, R.S., Morwal, S.B., Padma kumari, B., Konwar, M., Deshpande,  
 905 C.G., Joshi, R.R., Bhalwankar, R.V., Pandithurai, G., Safai, P.D., Narkhedkar, S.G.,

906 Dani, K.K., Nath, A., Nair, Sathy, Sapre, V.V., Puranik, P.V., Kandalgaonkar, S.S.,  
 907 Mujumdar, V.R., Khaladkar, R.M., Vijaykumar, R., Prabha, T.V., Goswami, B.N., The  
 908 Cloud Aerosol Interaction and Precipitation Enhancement Experiment (CAIPEEX):  
 909 overview and preliminary results (2012), Curr. Sci., Vol.102, 2012, 413-425.

910 Labrador, L. J., Kuhlmann, R. von, and Lawrence, M. G.: The effects of lightning-produced  
 911  $\text{NO}_x$  and its vertical distribution on atmospheric chemistry: sensitivity simulations with  
 912 MATCH-MPIC, Atmos. Chem. Phys., 5, 1815–1834, 2005.

913 Lamsal, L. N., Martin, R. V., Padmanabhan, A., van Donkelaar, A., Zhang, Q., Sioris, C. E.,  
 914 Chance, K., Kurosu, T. P., and Newchurch, M. J.: Application of satellite observations  
 915 for timely updates to global anthropogenic  $\text{NO}_x$  emission inventories, Geophys. Res.  
 916 Lett., 38,L05810, doi:10.1029/2010GL046476, 2011.

917 Li, Q., Jiang, J. H., Wu, D. L., Read, W. G., Livesey, N. J., Waters, J. W., Zhang, Y., Wang, B.,  
 918 Filipiak, M. J., Davis, C. P., Turquety, S., Wu, S., Park R. J., Yantosca R. M., and Jacob  
 919 D. J.: Convective outflow of South Asian pollution: A global CTM simulation compared  
 920 with EOS MLS observations, Geophys. Res. Lett., 32, L14826,  
 921 doi:10.1029/2005GL022762, 2005.

922 Liang, Q., Rodriguez, J. M., Douglass, A. R., Crawford, J. H., Olson, J. R., Apel, E., Bian, H.,  
 923 Blake, D. R., Brune, W., Chin, M., Colarco, P. R., da Silva, A., Diskin, G. S.,  
 924 Duncan, B. N., Huey, L. G., Knapp, D. J., Montzka, D. D., Nielsen, J. E., Pawson, S.,  
 925 Riemer, D. D., Weinheimer, A. J., and Wisthaler, A.: Reactive nitrogen, ozone and ozone  
 926 production in the Arctic troposphere and the impact of stratosphere-troposphere  
 927 exchange, Atmos. Chem. Phys., 11, 13181-13199, doi:10.5194/acp-11-13181-2011,  
 928 2011.

929 Liu, C., and Zipser E. J.: Global distribution of convection penetrating the tropical tropopause, J.  
 930 Geophys. Res., 110, D23104, 2005.

931 Martin, R. V., Sauvage, B., Folkins, I., Sioris, C. E., Boone, C., Bernath, P., and Ziemke, J.:  
 932 Space-based constraints on the production of nitric oxide by lightning, *J. Geophys. Res.*,  
 933 112, D09309, doi:10.1029/2006JD007831, 2007.

934 Miyazaki, K., Eskes, H. J., and Sudo, K.: Global NO<sub>x</sub> emission estimates derived from an  
 935 assimilation of OMI tropospheric NO<sub>2</sub> columns, *Atmos. Chem. Phys.*, 12, 2263–2288,  
 936 doi:10.5194/acp-12-2263-2012, 2012.

937 Murray, L. T., Jacob, D. J., Logan, J. A., Hudman, R. C., and Koshak, W. J.: Optimized regional  
 938 and interannual variability of lightning in a global chemical transport model constrained  
 939 by LIS/OTD satellite data, *J. Geophys. Res.*, 117, D20307, doi:10.1029/2012JD017934,  
 940 2012.

941 O'Sullivan D. W., • Heikes B. G Lee., M., Chang W., Gregory G. L., • Blake D. R., and Sachs  
 942 G. W., Distribution of hydrogen peroxide and methylhydroperoxide over the Pacific and  
 943 South Atlantic Oceans, *J. Geophys. Res.*, 104, D5, 5635-5646, 1999.

944 Pan L. L., A. Kunz, C. R. Homeyer , L. A. Munchak, D. E. Kinnison , and S. Tilmes,  
 945 Commentary on using equivalent latitude in the upper troposphere and lower  
 946 stratosphere, *Atmos. Chem. Phys.*, 12, 9187–9199, doi:10.5194/acp-12-9187-2012 ,  
 947 2012,

948 Park M., Randel W. J., Gettleman, A., Massie, S. T., and Jiang, J. H.: Transport above the  
 949 Asian summer monsoon anticyclone inferred from Aura Microwave Limb Sounder  
 950 tracers, *J. Geophys. Res.*, 112, D16309, doi:10.1029/2006JD008294, 2007.

951 Park, M., Randel, W. J., Emmons, L. K., and Livesey, N. J.: Transport pathways of carbon  
 952 monoxide in the Asian summer monsoon diagnosed from Model of Ozone and Related  
 953 Tracers (MOZART), *J. Geophys. Res.*, 114, D08303, doi:10.1029/2008JD010621, 2009.

954 Park, M., Randel, W. J., Kinnison, D. E., Garcia, R. R., and Choi, W.: Seasonal variation of  
 955 methane, water vapour, and nitrogen oxides near the tropopause: Satellite observations  
 956 and model simulations, *J. Geophys. Res.*, doi:10.1029/2003JD003706, 109, D03302,  
 957 2004.

958 Penki, R. K. and Kamra, A. K.: Lightning distribution with respect to the monsoon trough  
 959 position during the Indian summer monsoon season, *J. Geophys. Res.*, 118, 4780–4787,  
 960 doi:10.1002/jgrd.50382, 2013.

961 Pozzoli, L., Bey, I., Rast, J. S., Schultz, M. G., Stier, P., and Feichter, J.: Trace gas and aerosol  
 962 interactions in the fully coupled model of aerosol-chemistry-climate ECHAM5-  
 963 HAMMOZ: 1. Model description and insights from the spring 2001 TRACE-P  
 964 experiment, *J. Geophys. Res.*, 113, D07308, doi:10.1029/2007JD009007, 2008a.

965 Pozzoli, L., Bey, I., Rast, J. S., Schultz, M. G., Stier, P., and Feichter, J.: Trace gas and aerosol  
 966 interactions in the fully coupled model of aerosol-chemistry-climate ECHAM5-  
 967 HAMMOZ: 2. Impact of heterogeneous chemistry on the global aerosol distributions, *J.*  
 968 *Geophys. Res.*, 113, D07309, doi:10.1029/2007JD009008, 2008b.

969 Pozzoli, L., Janssens-Maenhout, G., Diehl, T., Bey, I., Schultz, M. G., Feichter, J., Vignati, E.,  
 970 and Dentener, F.: Re-analysis of tropospheric sulfate aerosol and ozone for the period  
 971 1980–2005 using the aerosol-chemistry-climate model ECHAM5-HAMMOZ, *Atmos.*  
 972 *Chem. Phys.*, 11, 9563-9594, doi:10.5194/acp-11-9563-2011, 2011.

973 Prabha T.V., Khain A., Maheshkumar R.S., Pandithurai G., Kulkarni J.R., Goswami B.N.  
 974 (2011), Microphysics of Premonsoon and Monsoon Clouds as Seen from In Situ  
 975 Measurements during the Cloud Aerosol Interaction and Precipitation Enhancement  
 976 Experiment (CAIPEEX), **J. Atm. Sc.**, Vol.68 , 2011, DOI: 10.1175/2011JAS3707.1,  
 977 1882-1901

978 Price, C. and Asfur, M.: Inferred long term trends in lightning activity over Africa, *Earth Planets*  
 979 *Space*, 58, 1197–1201, 2006.

980 Ranalkar, M. R and Chaudhari, H. S.: Seasonal variation of lightning activity over the Indian  
 981 subcontinent. *Meteorology and Atmospheric Physics*. 104, 125–134, 2009.

982 Randel, W. J. and Park, M.: Deep convective influence on the Asian summer monsoon  
 983 anticyclone and associated tracer variability observed with Atmospheric Infrared Sounder  
 984 (AIRS), *J. Geophys. Res.*, 111, D12314, doi:10.1029/2005JD006490, 2006.  
 985 Randel, W. J., Moyer, E., Park, M., Jensen, E., Bernath, P., Walker, K., and Boone C.: Global  
 986 variations of HDO and HDO/H<sub>2</sub>O ratios in the upper troposphere and lower stratosphere  
 987 derived from ACE-FTS satellite measurements, *J. Geophys. Res.*, 117, D06303,  
 988 doi:10.1029/2011JD016632, 2012.

989 Randel, W. J., Park, M., Emmons, L., Kinnison, D., Bernath, P., Walker, K. A., Boone, C. and  
 990 Pumphrey H.: Asian monsoon transport of pollution to the stratosphere, *Science*. Apr  
 991 30,328(5978),611-3. Epub Mar 25, 2010.

992 Rast, S., M.G. Schultz, I. Bey, T. van Noije and co-authors, Evaluation of the tropospheric  
 993 chemistry general circulation model ECHAM5–MOZ and its application to the analysis  
 994 of the chemical composition of the troposphere with an emphasis on the late RETRO  
 995 period 1990–2000 Technical rapport: 2014, Max Planck Institute of Meteorology, Earth  
 996 System Science, 74p. Real, E., Orlandi, E., Law, K. S., Fierli, F., Josset, D., Cairo, F.,  
 997 Schlager, H., Borrmann, S., Kunkel, D., Volk, C. M., McQuaid, J. B., Stewart, D. J., Lee,  
 998 J., Lewis, A. C., Hopkins, J. R., Ravegnani, F., Ulanovski A. and Liousse C.: Cross-  
 999 hemispheric transport of central African biomass burning pollutants: implications for  
 1000 downwind ozone production, *Atmos. Chem. Phys.*, 10, 3027–3046, 2010.

1001 Ridley, B. A., Madronich, S., Chatfield, R. B., Walega, J. G., Shetter, R. E., Carroll, M. A.,  
 1002 and Montzka D. D: Measurements and model simulations of the photostationary state  
 1003 during the Mauna Loa Observatory Photochemistry Experiment: Implications for radical  
 1004 concentrations and ozone production and loss rates, *J. Geophys. Res.*, 97(D10), 10375–  
 1005 10388, doi:10.1029/91JD02287, 1992.

1006 Ridley, B.A., J.G. Walega, J.E. Dye, and F.E. Grahek, Distributions of NO, NO<sub>x</sub>, NO<sub>y</sub>, and O<sub>3</sub> to  
 1007 12 km altitude during the summer monsoon season over New Mexico, *J. Geophys. Res.*,  
 1008 99, 25,519-25,534, 1994.

1009 Roeckner, E., Bauml, G., Bonaventura, L., Brokopf, R., Esch, M., Giorgetta, M., Hagemann, S.,  
 1010 Kirchner, I., Kornblueh, L., Manzini, E., Rhodin, A., Schlese, U., Schulzweida, U., and  
 1011 Tompkins, A.: The atmospheric general circulation model ECHAM5: Part 1, Tech. Rep.  
 1012 349, Max Planck Institute for Meteorology, Hamburg, 2003.

1013 Sander, S. P. Fried, R. R., Barker, J. R., Golden, D. M., Kurylo, M. J., Wine, P. H., J. Abbatt P.  
 1014 D., Burkholder, J. B., Kolb, C. E., Moortgat, G. K., Huie, R. E., Orkin, V. L.: Chemical  
 1015 kinetics and photochemical data for use in atmospheric studies, evaluation number 14,  
 1016 JPL Publ. 02-25, Jet Propul. Lab., Calif. Inst. of Technol., Pasadena. (Available  
 1017 at [http://jpldataeval.jpl.nasa.gov/pdf/JPL\\_02-25\\_rev02.pdf](http://jpldataeval.jpl.nasa.gov/pdf/JPL_02-25_rev02.pdf)), 2003.

1018 Schmitz, J. T., Mullen S. L., 1996: Water Vapor Transport Associated with the Summertime  
 1019 North American Monsoon as Depicted by ECMWF Analyses. *J. Climate*, **9**, 1621–1634.,  
 1020 1996.

1021 Schultz, M., Backman, L., Balkanski, Y., Bjoerndalsaeter, S., Brand, R., Burrows, J., Dalsoeren,  
 1022 S., de Vasconcelos, M., Grodtmann, B., Hauglustaine, D., Heil, A., Hoelzemann, J.,  
 1023 Isaksen, I., Kaurola, J., Knorr, W., Ladstaetter-Weienmayer, A., Mota, B., Oom, D.,  
 1024 Pacyna, J., Panasiuk, D., Pereira, J., Pulles, T., Pyle, J., Rast, S., Richter, A., Savage, N.,  
 1025 Schnadt, C., Schulz, M., Spessa, A., Staehelin, J., Sundet, J., Szopa, S., Thonicke, K., van  
 1026 der Bolscher, M., van Noije, T., van Velthoven, P., Vik, A., and Wittrock, F.: REanalysis  
 1027 of the Tropospheric chemical composition over the past 40 years (RETRO). A long-  
 1028 term global modeling study of tropospheric chemistry. Final Report, Tech. rep., Max  
 1029 Planck Institute for Meteorology, Hamburg, Germany, 2007.

1030 Schultz, M. G., Heil, A., Hoelzemann, J. J., Spessa, A., Thonicke, K., Goldammer, J. G., Held,  
 1031 A. C., Pereira, J. M. C., and van het Bolscher, M.: Global wildland fire emissions from  
 1032 1960 to 2000, *Global Biogeochem. Cy.*, 22, GB2002, doi:10.1029/2007GB003031, 2008  
 1033 Schultz, M.G., T. Pulles, R. Brand, M. Van het Bolscher and S.T. Dalsøren, , A global data set of  
 1034 anthropogenic CO, NO<sub>x</sub>, and NMVOC emissions for 1960-2000, in preparation and  
 1035 available at <http://eccad.sedoo.fr/>  
 1036 Schultz, M.G, A. Heil, J.J. Hoelzemann, A. Spessa, K. Thonicke, J. Goldammer, A.C. Held, J.M.  
 1037 Pereira, M. Van Het Bolscher, 2005: Global Wildland Fire Emissions from 1960 to 2000,  
 1038 doi:10.1029/2007GB003031 , *Global Biogeochemical Cycles* 22 (GB2002) : 17 PP  
 1039 Schumann, U. and Huntrieser, H.: The global lightning-induced nitrogen oxides source, *Atmos.*  
 1040 *Chem. Phys.*, 7, 3823–3907, 2007.  
 1041 Shepon, A., Gildor, H., Labrador, L. J., Butler, T., Ganzeveld, L. N., and Lawrence, M. G.:  
 1042 Global reactive nitrogen deposition from lightning NO<sub>x</sub>, *J. Geophys. Res.*, 112, D06304,  
 1043 doi:10.1029/2006JD007458, 2007.  
 1044 Singh, H. B., Viezee, W., Chen, Y., Thakur, A. N., Kondo, Y. and Talbot, R. W., Gregory, G. L.,  
 1045 Sachse, G. W., Blake, D. R., Bradshaw, J. D., Wang, Y., and Jacob D. J.: Latitudinal  
 1046 distribution of reactive nitrogen in the free troposphere over the Pacific Ocean in late  
 1047 winter/early spring, *J. Geophys. Res.*, 103(D21), 28237–28246, doi:10.1029/98JD01891,  
 1048 1998.  
 1049 Singh, H. B., Reactive nitrogen in the troposphere, *Environ. Sci. Technol.*, 21(4), 320–327, 1987

1050 Singh, H.B., Salas, L.J. and Viezee, W.: Global distribution of peroxyacetyl nitrate, *Nature*, Jun  
 1051 5-11;321(6070):588-91, 1986.

1052 Singh, H. B., Brune W. H., Crawford J. H., Jacob D. J., and Russell P. B.: Overview of the  
 1053 summer 2004 Intercontinental Chemical Transport Experiment – North America  
 1054 (INTEX-A), *J. Geophys. Res.*, 111, 2006, D24S01, doi:10.1029/2006JD007905.

1055 Stier, P., Feichter, J., Kinne, S., Kloster, S., Vignati, E., Wilson, J., Ganzeveld, T., Tegen, I.,  
 1056 Werner, M., Balkanski, Y., Schulz, M., Boucher, O., Minikin, A., and Petzold, A.: The  
 1057 aerosol climate model ECHAM5-HAM, *Atmos. Chem. Phys.* 5, 1125– 1165,  
 1058 doi:10.5194/acp-5-1125-2005, 2005.

1059 Talbot, R. W., Dibb, J. E., Scheuer, E. M., Bradshaw, J. D., Sandholm, S. T., Singh, H. B.,  
 1060 Blake, D. R., Blake, N. J., Atlas, E., and Flocke, F.: Tropospheric reactive odd nitrogen  
 1061 over the South Pacific in austral springtime, *J. Geophys. Res.*, 105, 6681–6694,  
 1062 doi:10.1029/1999JD901114, 2000.

1063 Talukdar, R. K., Burkholder, J. B., Schmoltner, A., Roberts, J. M., Wilson, R. R. and  
 1064 Ravishankara, A. R.: Investigation of loss processes for peroxyacetyl nitrate in the  
 1065 atmosphere: UV photolysis and reaction with OH, *J. Geophys. Res.*, 100, 14163–14173,  
 1066 1995.

1067 Tang, J. H., Chan, L. Y., Chang, C. C., Liu, S., and Li, Y. S.: Characteristics and sources of non-  
 1068 methane hydrocarbons in background atmospheres of eastern, southwestern, and southern  
 1069 China, *J. Geophys. Res.*, 114, D03304, doi:10.1029/2008JD010333, 2009.

1070 Tereszchuk K. A., Moore D. P., Harrison J. J., Boone C. D., Park M., Remedios J. J., Randel W.  
 1071 J., and Bernath P. F., Observations of peroxyacetyl nitrate (PAN) in the upper  
 1072 troposphere by the Atmospheric Chemistry Experiment/Fourier Transform Spectrometer  
 1073 (ACE-FTS), *Atmos. Chem. Phys.*, 13, 5601–5613, doi:10.5194/acp-13-5601-2013, 2013.

1074 Tie, X.X., Zhang, R., Brasseur, G., Emmons, L. and Lei, W.: Effects of lightning on reactive  
 1075 nitrogen and nitrogen reservoir species in the troposphere. *Journal of Geophysical*  
 1076 *Research-Atmospheres*, **106**, 3167-3178, DOI: 10.1029/2000JD900565, 2001.



1077 Uppala S. M., Kållberg P. W., Simmons A. J.<sup>\*</sup>, Andrae U., Costa Bechtold V. Da, Fiorino  
 1078 M., Gibson J. K., Haseler J., Hernandez A., Kelly G. A., Li X., Onogi K., Saarinen  
 1079 S., Sokka N., Allan R. P., Andersson E., Arpe K., Balmaseda M. A., Beljaars A. C.  
 1080 M., Berg L. Van De, Bidlot J., Bormann N., Caires S., Chevallier F., Dethof A.,  
 1081 Dragosavac M., Fisher M., Fuentes M., Hagemann S., Hólm E., Hoskins B. J.,  
 1082 Isaksen L., Janssen P. A. E. M., Jenne R., McNally A. P., Mahfouf J.-F., Morcrette J.-  
 1083 J., Rayner N. A., Saunders R. W., Simon P., Sterl A., Trenberth K. E., Untch A.,  
 1084 Vasiljevic D., Viterbo P. and Woollen J.,  
 1085 The ERA-40 re-analysis, *Q. J. R. Meteorol. Soc.*, 131(612), 2961–3012, doi:10.1256/qj.04.176,  
 1086 2005.  
 1087 Vaughan G. and Timmis C.: Transport of near-tropopause air into the lower midlatitude  
 1088 stratosphere, *Q. J. R. Meteorol. SOC.*, 124, pp. 1559-1578, 1998.  
 1089 Von Clarmann, T., Höpfner, M., Kellmann, S., Linden, A., Chauhan, S., Funke, B., Grabowski,  
 1090 U., Glatthor, N., Kiefer, M., Schieferdecker, T., Stiller, G. P., and Versick, S.: Retrieval of  
 1091 temperature, H<sub>2</sub>O, O<sub>3</sub>, HNO<sub>3</sub>, CH<sub>4</sub>, N<sub>2</sub>O, ClONO<sub>2</sub> and ClO from MIPAS reduced  
 1092 resolution nominal mode limb emission measurements, *Atmos. Meas. Tech.*, 2, 159–175,  
 1093 doi:10.5194/amt-2- 2159-2009, 2009.  
 1094 Wiegele A., Glatthor N., Hopfner M., Grabowski U., Kellmann S., Linden A., Stiller G., and von  
 1095 Clarmann T.: Global distributions of C<sub>2</sub>H<sub>6</sub>, C<sub>2</sub>H<sub>2</sub>, HCN, and PAN retrieved from MIPAS  
 1096 reduced spectral resolution measurements, *Atmos. Meas. Tech.*, 5, 723–734,  
 1097 doi:10.5194/amt-5-723-2012, 2012,  
 1098 Xiong, X., Houweling, S., Wei, J., Maddy, E., Sun, F., and Barnett, C.: Methane plume over  
 1099 South Asia during the monsoon season: Satellite observation and model simulation,  
 1100 *Atmos. Chem. Phys.*, 9, 783– 794, 2009.  
 1101 Zhang, L., Jacob, D. J., Boersma, K. F., Jaffe, D. A., Olson, J. R., Bowman, K. W., Worden, J.  
 1102 R., Thompson, A. M., Avery, M. A., Cohen, R. C., Dibb, J. E., Flock, F. M., Fuelberg, H.  
 1103 E., L. Huey, G., McMillan, W.W., Singh, H. B., and Weinheimer, A. J.: Transpacific  
 1104 transport of ozone pollution and the effect of recent, Asian emission increases on air

1105           quality in North America: an integrated analysis using satellite, aircraft, ozonesonde, and  
1106           surface observations, *Atmos. Chem. Phys.*, 8, 6117–6136, 2008.

1107   Zhao, C., Wang, Y., Choi, Y., and Zeng, T.: Summertime impact of convective transport and  
1108           lightning NO<sub>x</sub> production over North America: modeling dependence on meteorological  
1109           simulations, *Atmos. Chem. Phys.*, 9, 4315–4327, 2009.

1110   Ziereis, H., H. Schlager, P. Schulte, P.F.J. van Velthoven, and F. Slemr, Distributions of NO,  
1111           NO<sub>x</sub>, and NO<sub>y</sub> in the upper troposphere and lower stratosphere between 28°N and 61°N  
1112           during POLINAT 2, *J. Geophys. Res.*, **105**, 3653, 2000.

1113

1114

1115 Table 1: Global aircraft measurements used for model evaluation.

Experiment	Date Frame	Species	Location
<u>POLINAT-2</u> (Falcon) Ziereis et al.2000	Sep 19-Oct 25, 1997	O <sub>3</sub> , NO <sub>x</sub>	Canary-Islands: LAT= 25°N, 35°N, LON=160°W, 170°W E-Atlantic: LAT= 35°N, 45°N, LON=150°W,160°W Europe: LAT= 45°N, 55°N, LON=5°E, 15°E Ireland: LAT=50°N, 60°N, LON= 165°W,175°W
<u>PEM-Tropics-A</u> (DC8) Talbot et al. (2000)	Aug 24-Oct 15, 1996	O <sub>3</sub> , NO <sub>x</sub> , HNO <sub>3</sub> , PAN	Christmas-Island: LAN= 0°, 10°N, LON=20°W, 40°W Easter-Island: LAT=-40°N, 20°S, LON=60°W, 80°W Fiji: LAT= 0°,10°S. LON= 170°E, 10°W Iawaii: LAT= 10°N, 30°N, LON= 10°W., 30°W Tahiti: LAT= 20°S, 0°, LON= 20°W, 50°W
<u>PEM-Tropics-A</u> (P3) O'Sullivan et al, 1999	Aug 15-Sep 26, 1996	O <sub>3</sub> , HNO <sub>3</sub>	Christmas-Island: LAT= 0°, 10°N, LON= 20°W, 40°W Easter-Island: LAT= 40°S, 20°S, LON= 60°W, 80°W Hawaii: LAT= 10°N, 30°N, LON= 10°W, 30°W Tahiti: LAT= 20°S, 0°, LON= 20°W, 50°W
<u>ABLE-3B</u> (Electra) Harriss et al.,1994	Jul 6-Aug 15, 1990	O <sub>3</sub> , NO <sub>x</sub> , HNO <sub>3</sub> , PAN	Labrador: LAT= 50°N, 55°N, LON= 120°W, 135°W Ontario: LAT= 45°N, 60°N, LON= 90°W, 100°W US-E-Coast: LAT= 35°N, 45°N, LON= 100°W, 110°W.
<u>CITE-3</u> (Electra) Hoell et al 1993	Aug 22-Sep 29, 1989	O <sub>3</sub> , NO <sub>x</sub>	Natal: LAT= 15°S.,5°N, LON= 145°W, 155°W Wallops: LAT= 30°N, 40°N, LON= 100°W, 110°W
<u>ELCHEM</u> (Sabreliner) Ridley et al.,1999	Jul 27-Aug 22, 1989	O <sub>3</sub> , NO <sub>x</sub>	New-Mexico: LAT=30°N, 35°N , LON= 70°W, 75°W
<u>ABLE-3A</u> (Electra) Harriss et al.,1992	Jul 7-Aug 17, 1988	O <sub>3</sub> , NO <sub>x</sub> ,PAN	Alaska: LAT= 55°N, 75°N, LON= 10°W, 25°W
<u>ABLE-2A</u> (Electra) Harris et al., 1988	Jul 12-Aug 13, 1985	O <sub>3</sub>	E-Brazil: LAT= 10°S, 0°, LON= 120°W, 135°W W-Brazil: LAT= 5°S, 0°, LON= 110°W, 120°W
<u>STRATTOZ-3</u> (Caravelle 116) Drummond et al., 1988	Jun 4-26, 1984	O <sub>3</sub>	Brazil: LAT= 20°S, 0°, LON= 135°W, 155°W Canary-Islands: LAT= 20N, 35N, LON= 160°W, 155°W E-Tropical-N-Atlantic: LAT= 0°, 20°N, LON=150W.,165W. England: LAT= 45°N, 60°N, LON= 10°E, 5°W Goose-Bay: LAT= 45°N, 60°N, LON= 110°W, 125°W Greenland: LAT= 60N, 70N, LON= 110W, 150W Iceland: LAT= 60N, 70N, LON= 150W, 155W NW-South-America: LAT=-5°N, 10°N, LON= 95°W, 115°W Puerto-Rico: LAT= 10°N, 25°N, LON= 110°W, 120°W S-South-America: LAT= 65S,45S, LON= 95W, 120W SE-South-America: LAT= 45°S, 20°S. LON= 115°W, 140°W. SW-South-America: LAT=-45°S,25°S, LON= 105°W, 112°W Spain: LAT= 35°N, 45°N, LON= 15W, 0° W-Africa: LAT= 0., 15°N, LON= 15°W, 0°. W-South-America: LAT= 25°S, 5°S. LON=

			95°W,110°W Western-N-Atlantic: LAT= 25°N, 45°N, LON= 110°W,120°W
<u>CITE-2</u> (Electra) Hoell et al., 1990	Aug 11-Sep 5, 1986	O <sub>3</sub> , NO <sub>x</sub> , HNO <sub>3</sub> , PAN	Calif: LAT= 35°N, 45°N, LON= 55°W, 70°W Pacific: LAT= 30°N, 45°N, LON= 45°W, 55°W
INTEX-A, Singh et al. (2006)	Jul–Aug 2004	O <sub>3</sub> , PAN, NO <sub>x</sub>	Eastern North America: LAT= 29°N, 51°N, Lon: 44°W-120°W
CAIPEEX (Prabha et al., 2011)	Sep 2010 –Oct 2010	O <sub>3</sub> , NO <sub>x</sub>	Lat=12°N,22°N, Lon=74°E, 78°E

1116

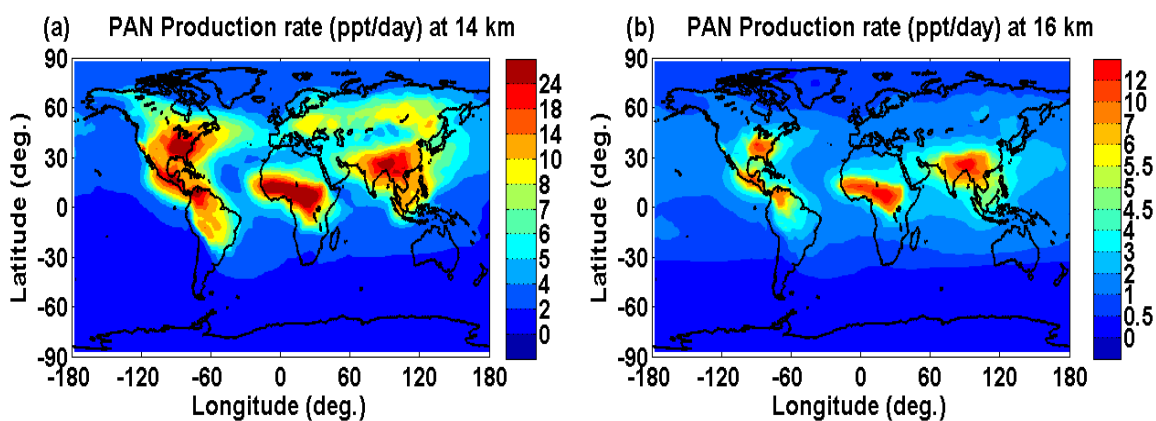


Figure 1. PAN production rates at (a) 14 km and (b) 16 km. Key regions of biomass burning and anthropogenic emissions of pollutants are evident and correspond to maxima in PAN production. Weaker dispersed background formation is evident as well.

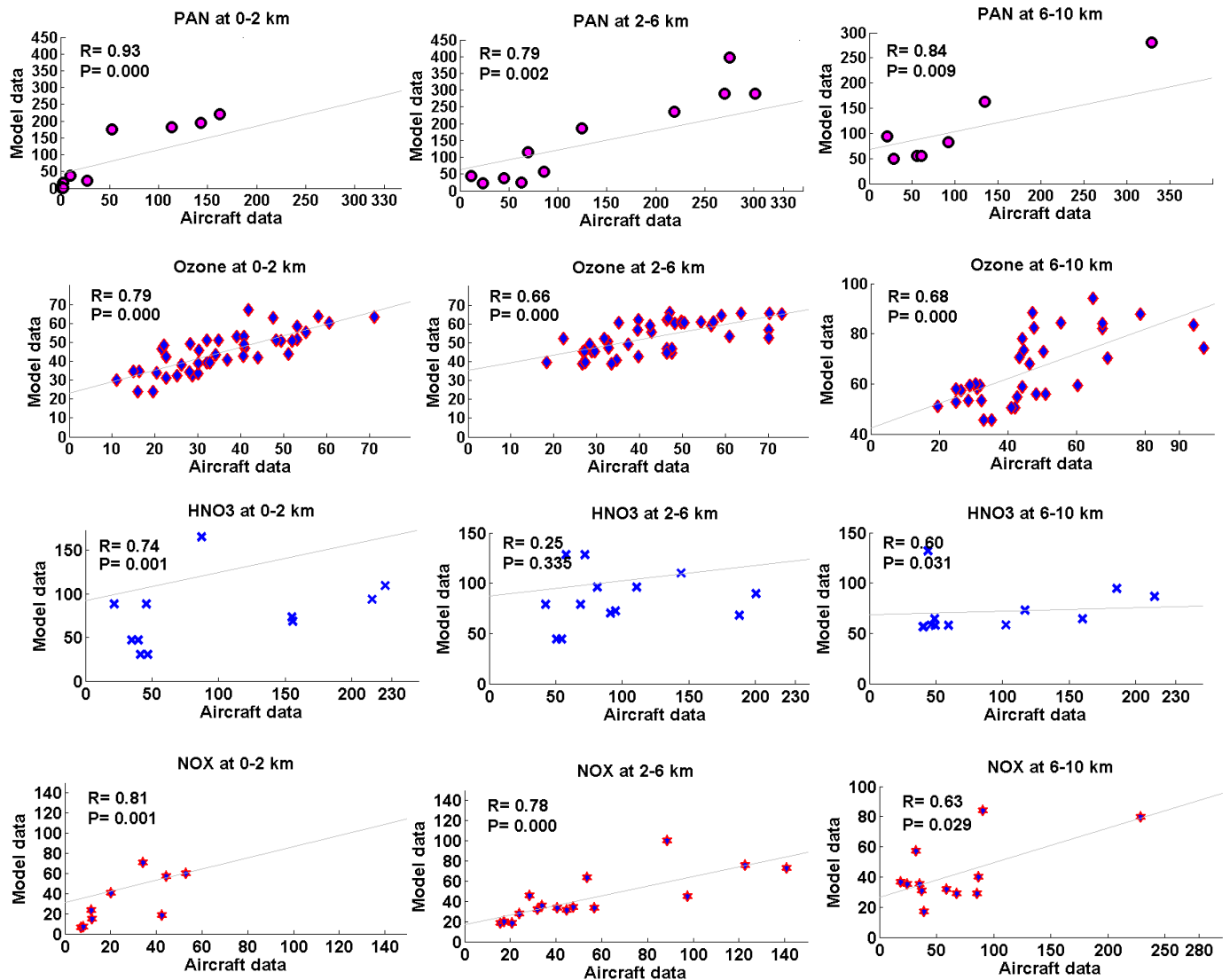


Figure 2. Scatter plot between model simulation (averaged for 1995-2004) and aircraft observations of PAN (ppt), ozone (ppb), HNO<sub>3</sub> (ppt), NO<sub>x</sub> (ppt) (averaged for the monsoon season (June-September)). The model simulations and aircraft observations are averaged for altitude ranges over the coherent regions. The Pearson's correlation coefficient (R) and corresponding p-value is given in each subplot.

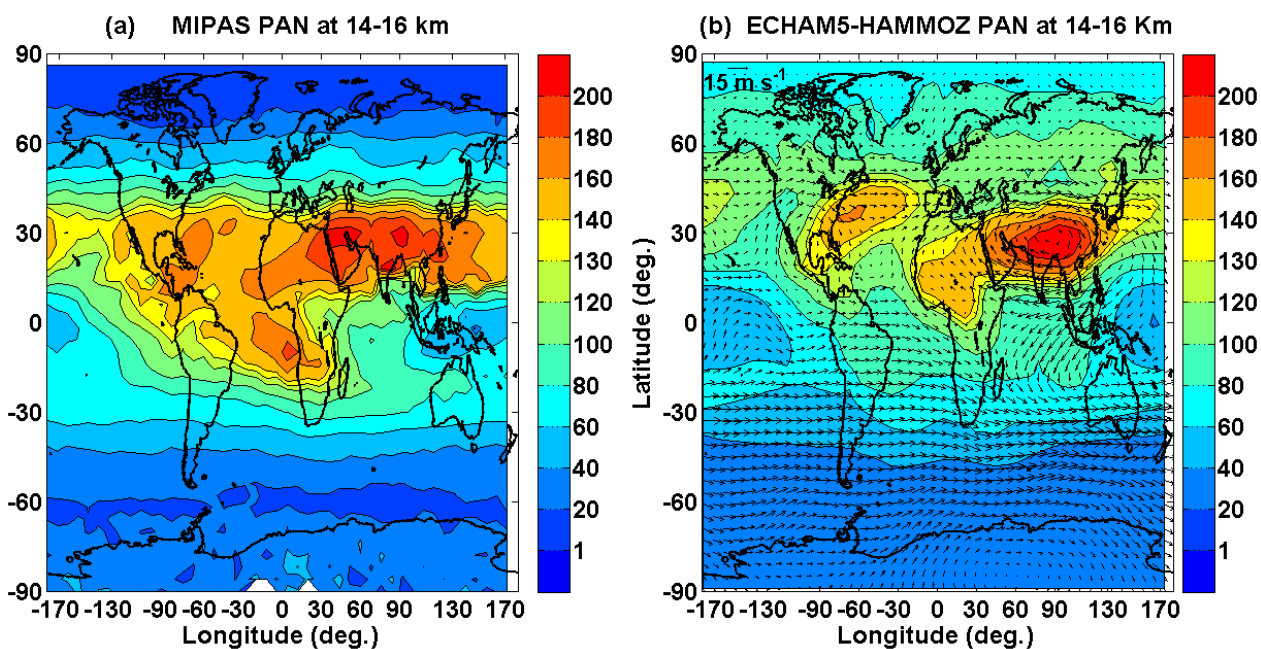


Figure 3. Distribution of seasonal mean PAN concentration (ppt) averaged for 14 -16 km (a) observed by MIPAS-E (climatology for the period 2002-2011) (b) ECHAM5-HAMMOZ CTRL simulations. Wind vectors at 16 km are indicated by black arrows in figures (b)

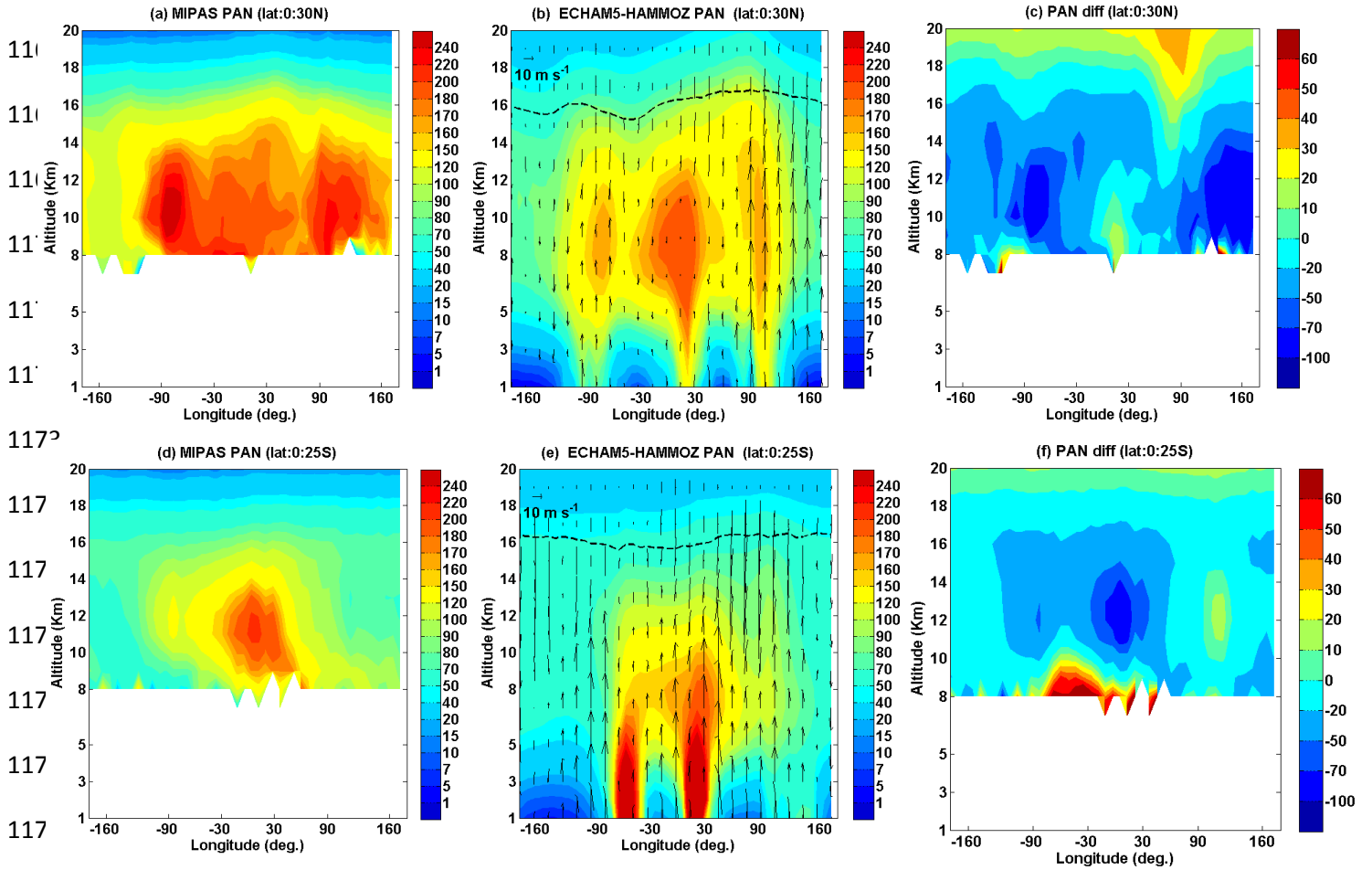


Figure 4. Longitude-altitude cross section of PAN (ppt) averaged for monsoon season and  $10^{\circ}\text{N}$  -  $30^{\circ}\text{N}$ ; (a) MIPAS-E climatology (b) ECHAM5-HAMMOZ CTRL simulations. (c) difference in PAN (ppt) (MIPAS - ECHAM5-HAMMOZ). PAN (ppt) averaged for monsoon season and  $0^{\circ}$  -  $25^{\circ}\text{S}$  (d) MIPAS-E climatology (e) ECHAM5-HAMMOZ CTRL simulations (f) difference in PAN (ppt) (MIPAS - ECHAM5-HAMMOZ). ECHAM5-HAMMOZ simulations are smoothed with averaging kernel of MIPAS-E. Wind vectors are indicated by black arrows in figures (b) and (e). The vertical velocity field has been scaled by 300. The black line in (b) and (e) indicates the tropopause.



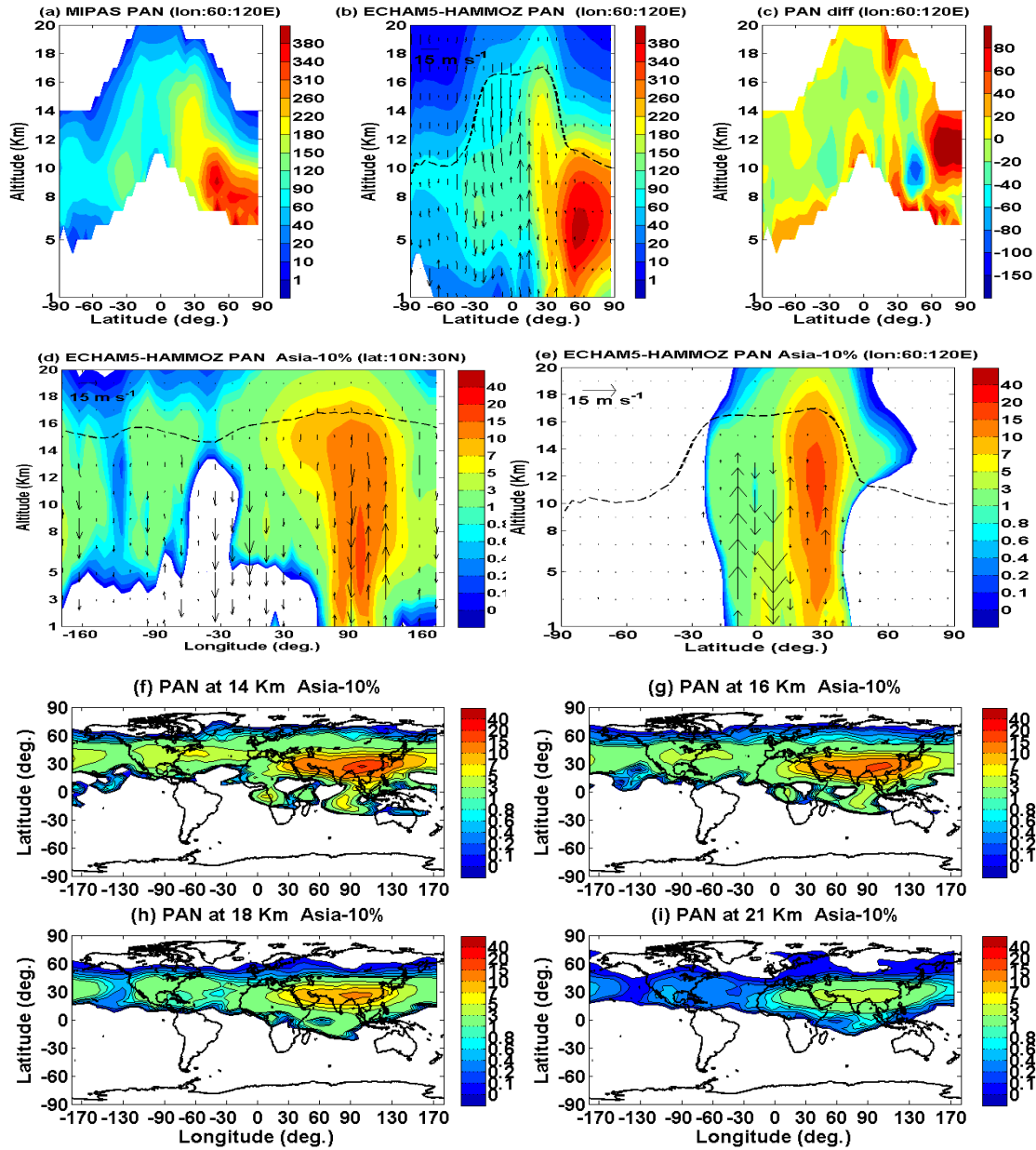


Figure 5. Latitude-altitude cross section of PAN (ppt) (a) MIPAS-E climatology, averaged for monsoon season and for 60-120°E, (b) PAN from ECHAM5-HAMMOZ CTRL simulations, averaged for monsoon season and 60-120°E, (c) difference in PAN (ppt) (MIPAS-ECHAM5-HAMMOZ), (d) longitude-altitude section averaged over 0-30°N obtained from reference-Asia-10% simulations (e) same as (d) but latitude-altitude section averaged over 60-120°E, (f) – (i) latitude-longitude sections of reference – Asia-10% simulations at 14 km, 16 km, 18 km, 21 km respectively. Wind vectors are indicated by black arrows. The vertical velocity field has been scaled by 300.

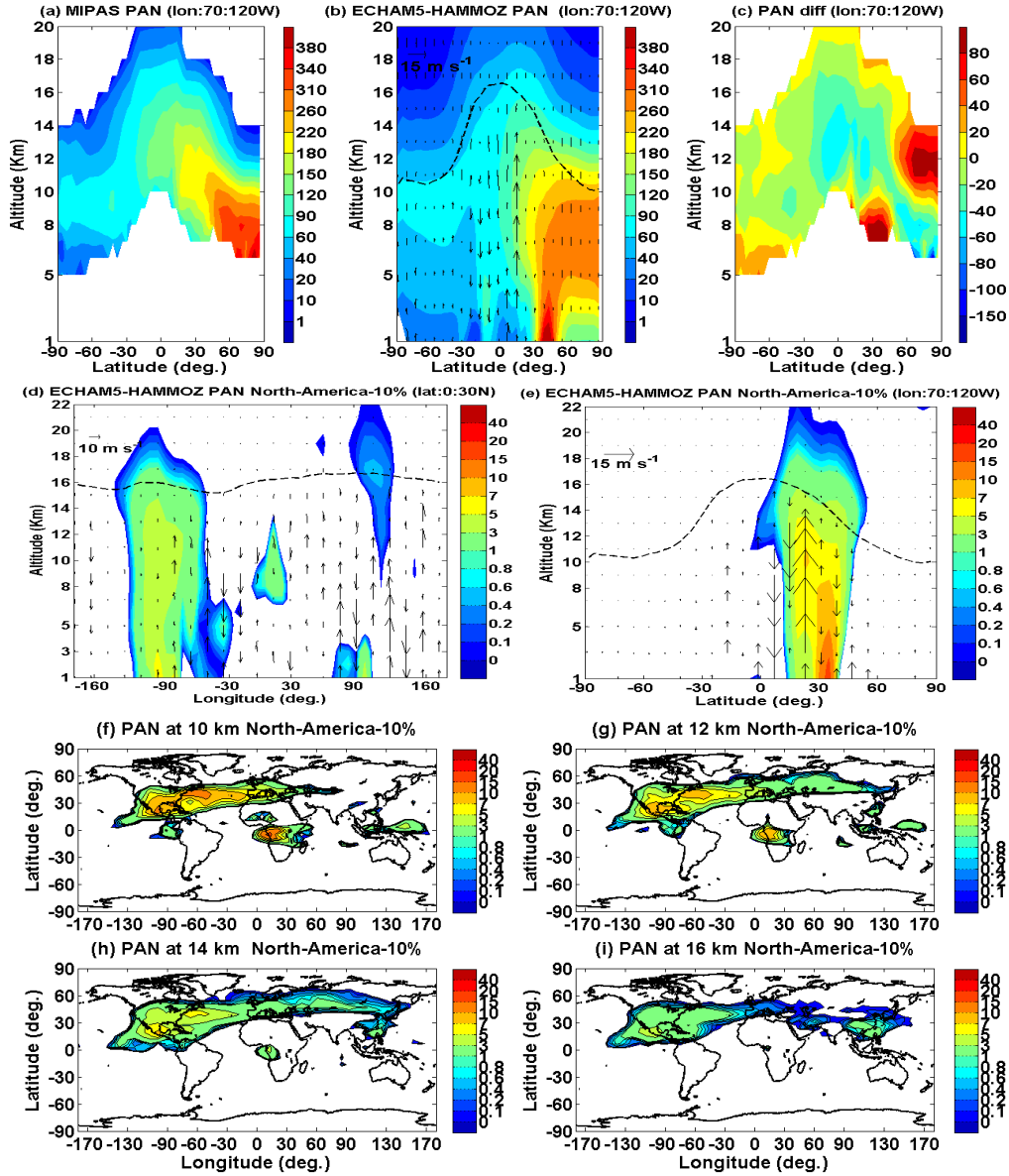


Figure 6. Latitude-altitude cross section of PAN (ppt) (a) MIPAS-E climatology, averaged for monsoon season and for 70-120° W, (b) PAN from ECHAM5-HAMMOZ CTRL simulations, averaged for monsoon season and 70-120° E, (c) difference in PAN (ppt) (MIPAS-ECHAM5-HAMMOZ), (d) longitude-altitude section averaged over 0-30° N obtained from reference-North-America-10% simulations (e) same as (d) but latitude-altitude section averaged over 120°W-70°W, (f)–(i) latitude-longitude sections of reference – North-America-10% simulations at 10km, 12 km 14km, 16 km respectively. Wind vectors are indicated by black arrows. The vertical velocity field has been scaled by 300.

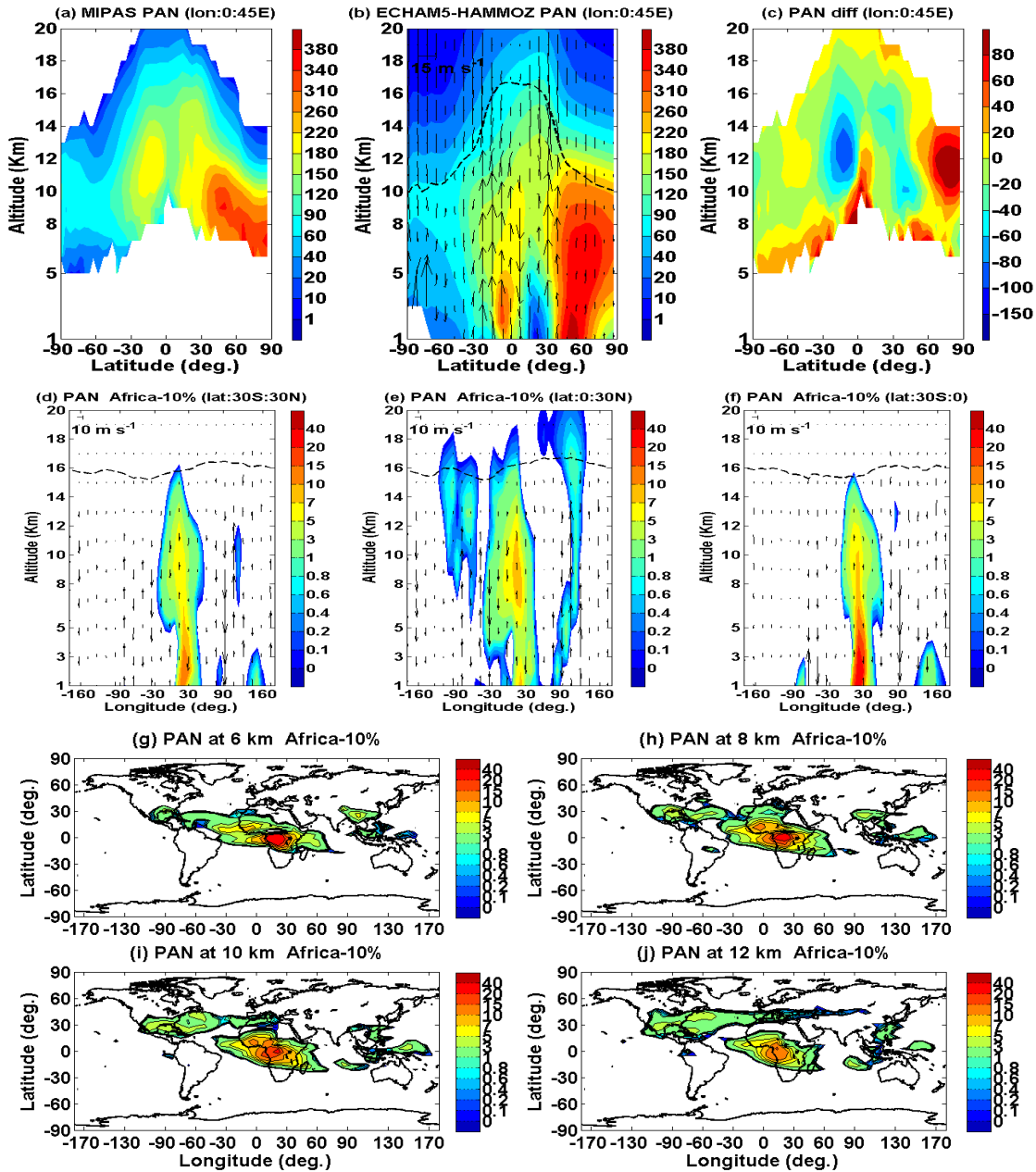


Figure 7. Latitude-altitude cross section of PAN (ppt) (a) MIPAS-E climatology, averaged for monsoon season and for 0-45° E, (b) PAN from ECHAM5-HAMMOZ CTRL simulations, averaged for monsoon season and 0-45° E, (c) difference in PAN (ppt) (MIPAS-ECHAM5-HAMMOZ), (d) longitude-altitude section averaged over 30°S - 30°N obtained from reference-Africa-10% simulations (e) same as d but averaged over 0-30°N, (f) same as d but averaged over 0-30°S. Wind vectors are indicated by black arrows. The vertical velocity field has been scaled by 300, Longitude – latitude section of PAN obtained from reference- Africa-10% simulations at (g) 6 km, (h) 8 km, (i) 10 km, (j) 12km.

1268

1269

1270

1271

1272

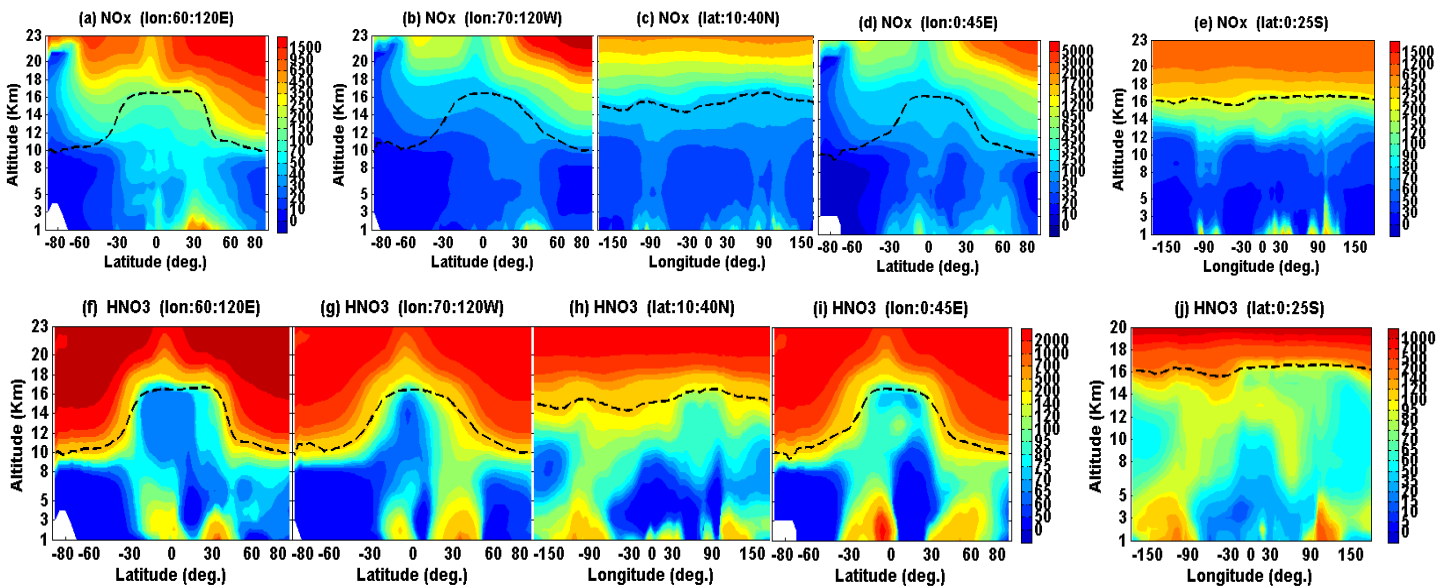
1273

1274

1275

1276

1277



1278

1279

1280

1281

1282

1283

1284

1285

1286

1287

1288

1289

1290

1291

Figure 8. Panel (a) Latitude-altitude cross section of seasonal mean ECHAM5-HAMMOZ  $\text{NO}_x$  (ppt) averaged for (a)  $60^\circ \text{E}$ - $120^\circ \text{E}$ , (b)  $70^\circ \text{W}$ - $120^\circ \text{W}$ , (c) longitude-altitude cross section averaged over  $10^\circ \text{N}$ - $40^\circ \text{N}$ , (d) latitude-altitude cross section averaged over  $0$ - $45^\circ \text{E}$  and (e) longitude-altitude cross section averaged over  $0$ - $25^\circ \text{S}$ , (f)-(i) same as (a)-(e) but for  $\text{HNO}_3$ .

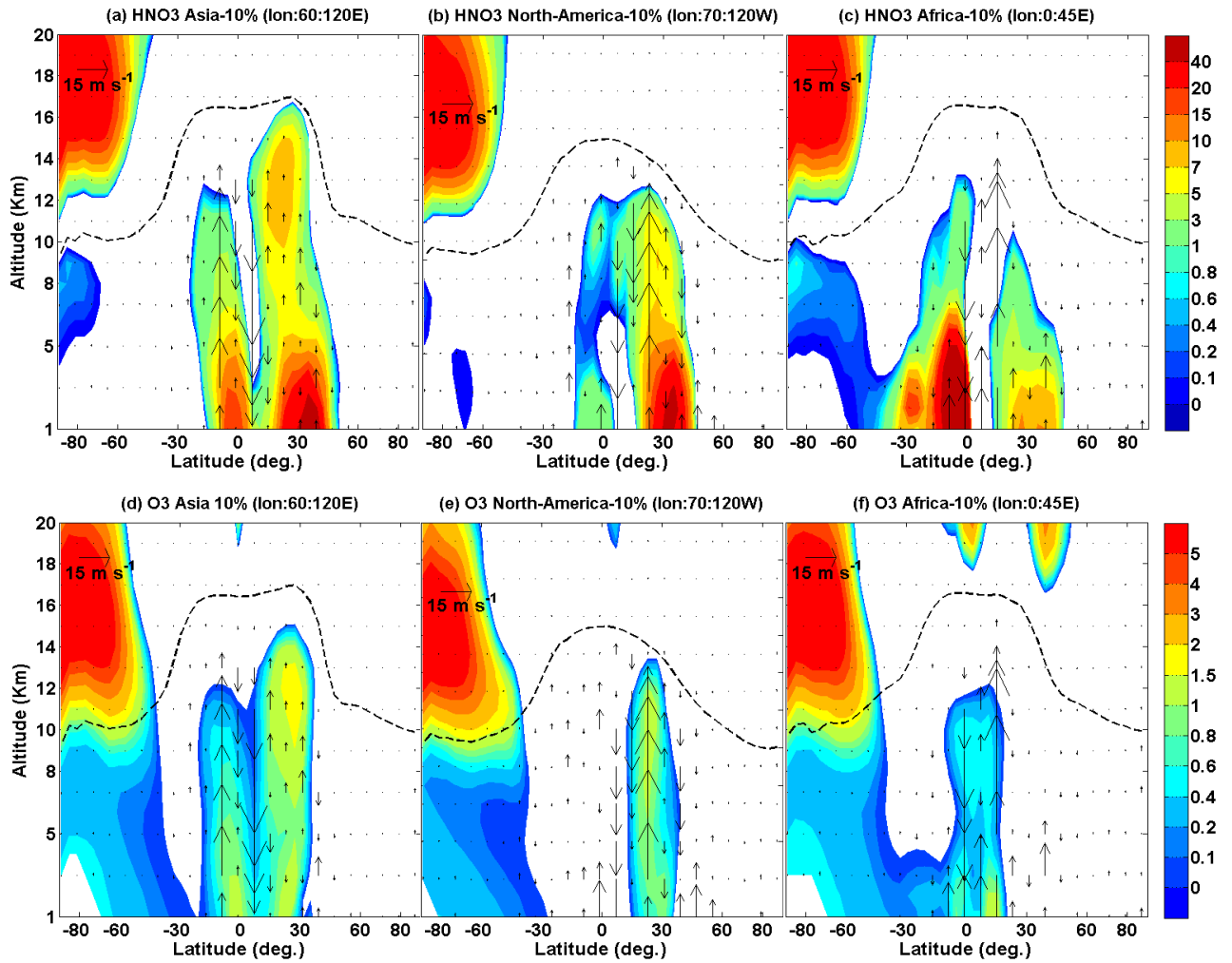


Figure 9. Latitude-altitude variation of (a)  $\text{HNO}_3$  (Reference – Asia-10%) , averaged over  $60^\circ$ - $120^\circ\text{E}$  (b)  $\text{HNO}_3$  (difference of Reference – North-America-10%) , averaged over  $70^\circ$ - $120^\circ\text{W}$  (c)  $\text{HNO}_3$  (Reference – Africa-10%), averaged over  $0$ - $45^\circ\text{E}$  (d)  $\text{O}_3$  (difference of Reference – Asia-10%) averaged over  $60$ - $120^\circ\text{E}$  (e)  $\text{O}_3$  (Reference – North-America-10%) over North America averaged over  $70^\circ$  - $120^\circ\text{W}$  (f)  $\text{O}_3$  (Reference – Africa-10%) over Africa averaged over  $0$ - $45^\circ\text{E}$  (Reference – Africa-10%) .  $\text{HNO}_3$  is expressed in ppt and ozone in ppb.

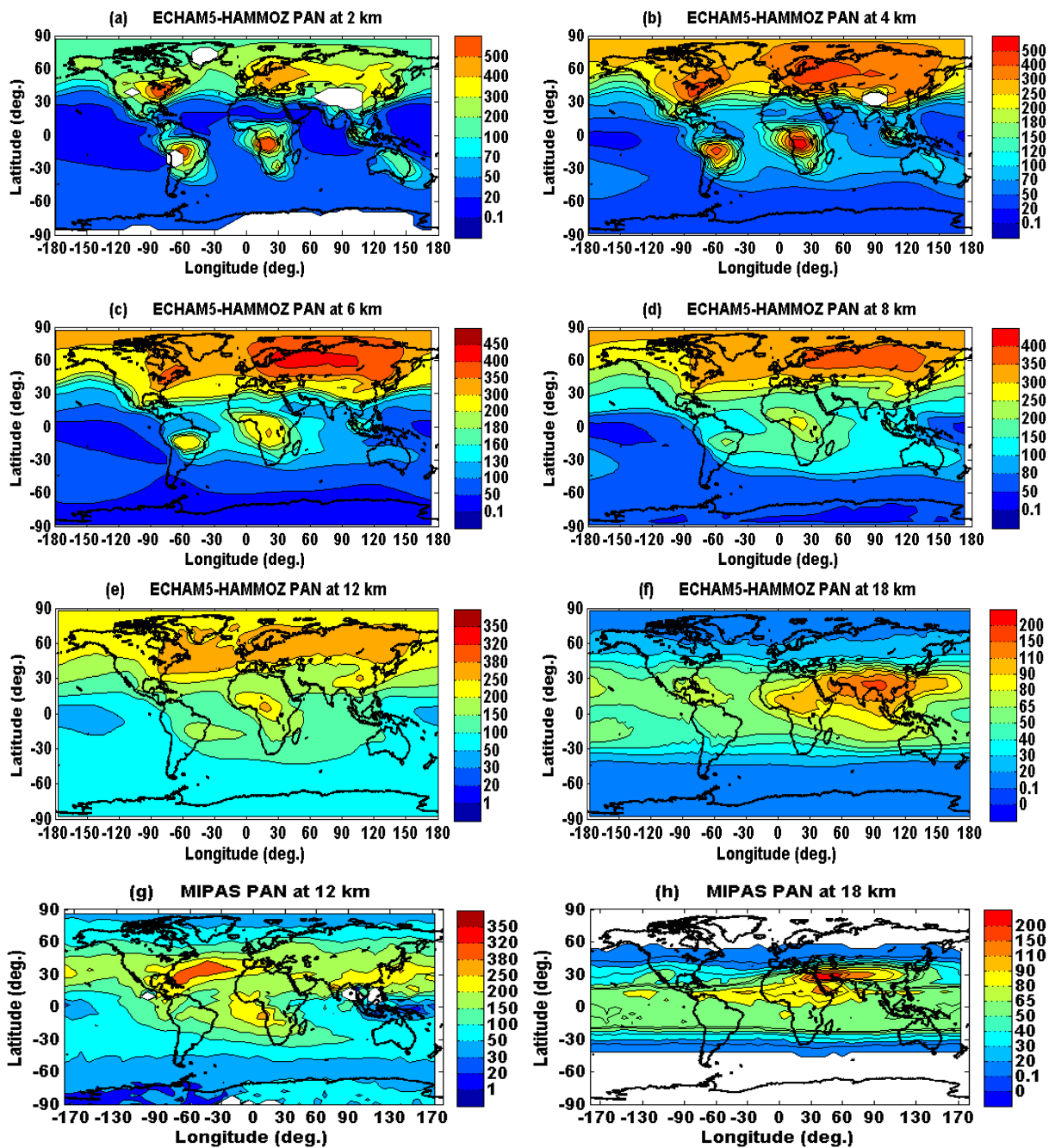


Figure 10. Latitude-longitude cross section of PAN (ppt) averaged for monsoon season (a) ECHAM5-HAMMOZ simulations at 2 km (b) 4 km (c) 6 km (d) 8 km (e) 12 km (f) 18 km. MIPAS-E climatology at (g) 12 km (h) 18 km.



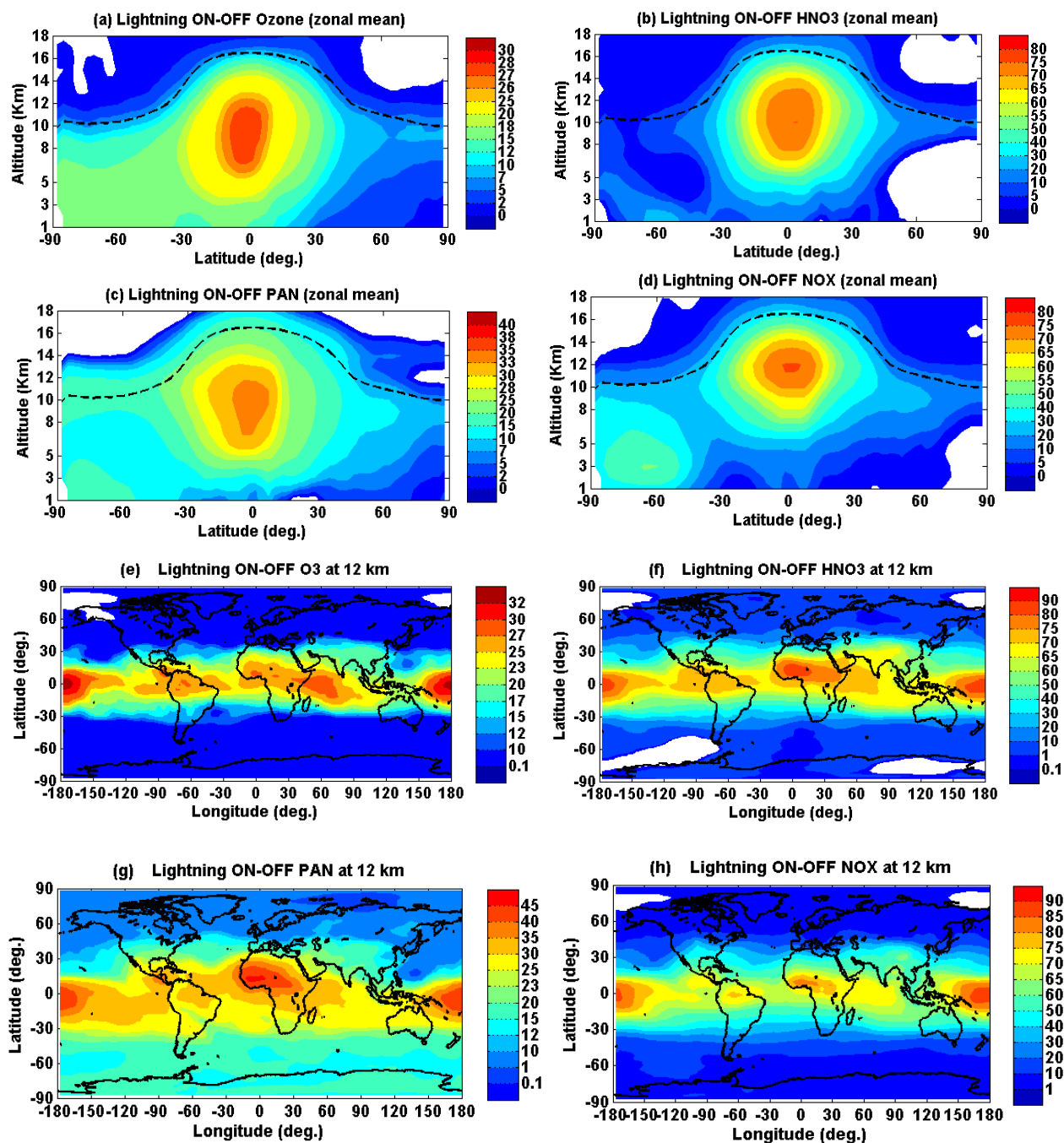


Figure 11. Zonal averaged seasonal mean changes (percentage) produced from lightning in (a) ozone (b) HNO<sub>3</sub> (c) PAN (d) NO<sub>x</sub>, distribution of seasonal mean changes (percentage) produced from lightning in (e) ozone (f) HNO<sub>3</sub> (g) PAN (h) NO<sub>x</sub> at 12 km.